Biophysical *Journal*
Article

Biophysical Society

Spatial control over near-critical-point operation ensures fidelity of ParAB*S*-mediated DNA partition

Longhua Hu,[1] Jérôme Rech,[2] Jean-Yves Bouet,[2,*] and Jian Liu[1,*]
[1]Center for Cell Dynamics, Department of Cell Biology, Johns Hopkins University School of Medicine, Baltimore, Maryland and [2]Laboratoire de Microbiologie et Génétique Moléculaires, Centre de Biologie Intégrative, Centre National de la Recherche Scientifique, Université de Toulouse, UPS, Toulouse, France

ABSTRACT In bacteria, most low-copy-number plasmid and chromosomally encoded partition systems belong to the tripartite ParAB*S* partition machinery. Despite the importance in genetic inheritance, the mechanisms of ParAB*S*-mediated genome partition are not well understood. Combining theory and experiment, we provided evidence that the ParAB*S* system—DNA partitioning in vivo via the ParA-gradient-based Brownian ratcheting—operates near a transition point in parameter space (i.e., a critical point), across which the system displays qualitatively different motile behaviors. This near-critical-point operation adapts the segregation distance of replicated plasmids to the half length of the elongating nucleoid, ensuring both cell halves to inherit one copy of the plasmids. Further, we demonstrated that the plasmid localizes the cytoplasmic ParA to buffer the partition fidelity against the large cell-to-cell fluctuations in ParA level. The spatial control over the near-critical-point operation not only ensures both sensitive adaptation and robust execution of partitioning but also sheds light on the fundamental question in cell biology: how do cells faithfully measure cellular-scale distance by only using molecular-scale interactions?

SIGNIFICANCE Sensitive response and robust execution of functions against uncertainties define a central theme of biological processes. Exploiting the widespread ParA-mediated bacterial partition as the model system, we present a general strategy to address this dichotomy. We show the low-copy-number plasmid "self-drives" by both localizing cytoplasmic ParA nearby and "creating" and "following" the ParA gradient on the nucleoid. The plasmid-localized activities combine to buffer against cellular fluctuations and operate near a critical point in the parameter space, which adapts the plasmid segregation distance to the cell length. This ensures the replicated plasmids always partition into the two different cell halves, maximizing partition fidelity. Spatial control over near-critical-point operation provides a mechanism that faithfully measure cellular-scale distance by using only molecular-scale interactions.

INTRODUCTION

Cellular processes must establish the right operating point in a very large parameter space that allows robust execution of biological function and simultaneously sensitive adaptation to environmental cues. What is the character of this right operating point? How do cells find and maintain it? It is postulated that all living systems operate near the edge of phase transition (1), i.e., near a critical point at which the system is halfway between two phases in its parameter space. This way, the system has the equal probability to operate in either of the two phases with the maximal susceptibility and displays large fluctuations with a diverging correlation length. Thus, operating near such a critical point could allow the system to sensitively and rapidly respond to changes in the environment. Indeed, there are increasing data—ranging from developmental biology to neuroscience—supporting this notion (2–5). For instance, patterns of gap gene expression in the early *Drosophila* embryo were reported to exhibit signatures of criticality, wherein the divergence of correlation length between gene expressions was proposed to adapt the spatial patterning to the embryo growth (3). Likewise, evidence suggested that neural systems operate at criticality teetering between stability and chaos that maximizes their information processing capacity (2). However, this evidence is largely statistical inference from experimental data and lack the physical mechanisms that give rise to the near-critical-point behavior. Crucially, it is unclear how cellular processes

Submitted February 3, 2021, and accepted for publication August 13, 2021.
*Correspondence: jean-yves.bouet@univ-tlse3.fr or jliu187@jhmi.edu
Editor: Anatoly Kolomeisky.
https://doi.org/10.1016/j.bpj.2021.08.022

maintain the robustness of operating near the critical point in the presence of ever-lasting noises (e.g., the fluctuations in gene expression at a single-cell level (6–8)). From this perspective, we set out to examine the physical mechanism of bacterial DNA segregation with the emphasis on how the operating point of DNA partition machinery is controlled to maximize the partition fidelity. We exploited low-copy-number plasmid partition in the bacteria as the model system by combining theoretical modeling with experimental testing.

Segregating replicated genomes before cell division is essential to ensure faithful genetic inheritance. Despite its simple form, partitioning of low-copy-number plasmids in bacteria is robust with an extremely low error rate (less than 0.1% per generation) (9) and provides a tractable paradigm to understand fundamental principles of genome segregation (10). Most low-copy-number plasmids are actively partitioned—by a conserved tripartite ParAB*S* system—along the nucleoid, a rod-like structure consisting primarily of condensed chromosomal DNA. Although cargo trafficking in vivo typically utilizes cytoskeletal filament or motor-protein-based mechanisms, the ParAB*S* machinery utilizes none of the conventional mechanisms for partitioning (11–14). How the ParAB*S* system drives genome partitioning has puzzled the field since its first postulation in the replicon theory (15).

The key elements of ParAB*S* system are as follows (10): ParA is an ATPase that binds nonspecifically to DNA in the nucleoid in an ATP-bound dimeric state. ParB is the adaptor protein. It binds specifically at a centromere-like site *parS* on the plasmid and sequence nonspecifically around *parS* to form large clusters called partition complexes (PCs). ParB regulates ParA DNA binding by 1) direct interaction that provokes its release from the nucleoid (13), and by 2) stimulating the ATPase activity that convert ParA in the ADP-bound form that do not bind nucleoid DNA (16,17). It is not understood how the chemical energy provided by ATP hydrolysis is harnessed to ensure the PC partition fidelity beside its important implication in separating newly duplicated *parS* sites (18).

Spatial-temporal features of the ParAB*S* system expose some clues of its inner workings. PCs move around and frequently switch directions over the cell length (11,19–23). Because the timing of PC replication and segregation is not directly coupled to cell cycle and the nucleoid itself keeps elongating before cell division (24–26), the replicated PCs can be anywhere along the nucleoid length when they start to split apart (22). Intriguingly, the replicated PCs always first move apart persistently and then position themselves with the separation being approximately half of the cell length (11,19,20,22,27). Although segregating by half of the cell length ensures the partition fidelity by always positioning the replicated PCs in the different cell halves, it precipitates the following questions. First, given that the PCs locally interact with the nucleoid, which elongates in proportion to the cell length (28), the question becomes: how do the PCs have the global "view" of and adapt their separation to the length of the elongating nucleoid and, ultimately, the half of the cell length? Second, what ensures the partition robustness in the presence of ever-lasting noises, e.g., the fluctuations in protein levels? Addressing these questions lay at the heart of one of the fundamental questions in cell biology: how do cells faithfully measure cellular-scale distance by only using molecular-scale interactions?

We previously established the ParA protein gradient-based Brownian ratchet model—a new mechanism of processive cargo transport without resorting to filament or conventional stepping motor proteins (e.g., myosins, kinesins, or dynein) (29,30). With multiple ParA-ParB bonds tethering a *parS*-coated cargo to a DNA carpet, ParB-stimulated bond dissociation triggers the release of the ParA from the DNA carpet, the randomness of which results in a force imbalance that drags the cargo forward. Critically, the time delay in resetting ParA DNA-binding affinity generates a ParA-depletion zone behind the forward-moving cargo (14,29,31), perpetuating the asymmetry and persistent movement. As such, the ParAB*S* system can work as a Brownian ratchet: the ParB-bound cargo "self-drives" by both creating and following a ParA gradient over the DNA. This protein gradient-based Brownian ratchet model provides a conceptual framework that allowed us to explain—for the first time, to our knowledge, in a coherent manner—the diverse motility patterns of PCs evidenced in vivo (32) and starts to gain support from in vivo experiments (33–36). However, our effort so far focused on a highly simplified picture, it is unclear 1) whether and how this Brownian ratchet mechanism can adapt the plasmid segregation distance to the length of an elongating nucleoid, and 2) how the PC partition ensures its fidelity against cellular noises.

Here, we show that 1) this ParA-gradient-based Brownian ratcheting of bacterial low-copy-number plasmid partitioning operates near a critical point in vivo, and 2) the spatial controls over the near-critical-point operation allow both sensitive adaptation of partition to the nucleoid length and robust execution of partition to buffer against noises.

MATERIALS AND METHODS

Bacterial strains and plasmids

Escherichia coli K-12 strains are derivatives of DLT1215 (37) and transformed with the plasmids pJYB240 (38), pJYB243 (39), or pJYB249 (38). Cultures were grown at 37°C with aeration in Luria-Bertany (LB) broth (40) containing thymine (10 μg.mL^{-1}) and antibiotics as appropriate: chloramphenicol (10 μg.mL^{-1}) and kanamycin (50 μg.mL^{-1}). For microscopy and plasmid stability assays, cultures were grown at 30°C with aeration in M9 minimal medium supplemented with 0.4% glycerol, 1 mM magnesium sulfate ($MgSO_4$), 0.1 mM calcium chloride ($CaCl_2$), 1 μg.mL^{-1} thiamine, 20 μg.mL^{-1} leucine, and 40 μg.mL^{-1} thymine supplemented or not with 0.2% casamino acids. The generation times in M9 Glycerol

(M9Gly) with or without 0.2% casamino acids are 45 or 242 min, respectively.

Plasmid stability assays for plasmid-copy-number determination

Experiments were started from colonies of *E. coli* cells carrying the plasmids under test. Overnight cultures in M9Gly, with or without casamino acids, containing chloramphenicol were diluted 250-fold into the same medium and grown to $A_{600} = 0.25$. Samples were then diluted serially into fresh medium without chloramphenicol and were processed as described previously (41). To determine the fraction of cells that retained the plasmid, samples were taken at the beginning and after 5, 10, 20, and 30 generations or after 25 generations for growth in the absence or presence of casamino acids, respectively. The loss frequency (f) per generation is calculated using the following formula: $f = 1 - (\text{cell carrying the F-plasmid/total cell})^{1/g}$, where g is the generation number, as previously described (39).

The plasmid copy number at cell division (n) is calculated from the probability of having one plasmid-free cell at cell division as a function of the copy number, $P_0 = 2^{(1-n)}$, from which we obtained the theoretical frequency of random loss per generation. The copy number per cell is ln2 (naperian logarithm) time n (19).

Epifluorescence microscopy and analysis

Overnight cultures were inoculated into fresh media at a concentration permitting at least 10 generations of exponential growth and incubated at 30°C to an optical density ($OD_{600\ nm}$) of ~0.25. Samples (0.7 μL) were deposited to the surface of a layer of 1% agarose buffered in M9 solution, as described (42). The cells were imaged at 30°C using an Eclipse Ti-E/B wide field epifluorescence microscope (Nikon, Tokyo, Japan) with a phase contrast objective (CFI Plan Apochromat LBDA 100× oil NA1.45; Nikon) and a Semrock filter YFP (Excitation: 500BP24; Dichroic mirror: 520; Emission: 542BP27; IDEX Health & Science, Rochester, NY) or fluorescein isothiocyanate (Ex: 482BP35; DM: 506; Em: 536BP40). Images were taken using an Andor Neo SCC-02124 camera (Oxford Instruments, Abingdon, UK) with illumination at 80% from a SpectraX source Led (Lumencor, Beaverton, OR) and exposure times of 0.2–1 s. Nis Elements AR software (Nikon) was used for image capture and editing. Image analyses were performed using ImageJ plugins. The average foci number per cell was measured using the "Cell Counter" plugins. Tracking the PC and nucleoid length was done in the MicrobeJ plugin (43,44). It involves finding the cells of interest and tuning the parameters in MicrobeJ to get the data. Specifically, for each identified cell, we recorded the length of the cell, integrated fluorescence of ParA, and the peak positions of ParB fluorescence intensity, which were then used to represent the positions of the PCs. We also recorded the fluorescence profile of the nucleoid along the long axis of the cell, from which the nucleoid length of the cell was derived using the full-width-half-height approach. For ParA-PC colocalization analysis, we used a self-developed (Centre de Biologie Intégrative) Python-based tool (Distance2MaxProfile: https://imaprocess.pythonanywhere.com/Analymage/detail_projet/20/).

RESULTS

Model development

Going beyond our previous modeling efforts (29,30,32), we built the in vivo model—to specifically capture how ParA-mediated PC partition responds to the dynamical changes—associated with nucleoid elongation during cell growth. The qualitative model features are described below (Fig. 1), followed by the quantitative mathematical formulation.

Our model begins with two PCs arranged side-by-side to mimic the replicated PCs and examines the subsequent partition dynamics. As a starting point of the modeling, we depict each PC as a circular disk of ~100 nm in radius (34,39), the nucleoid as a flat rectangle, and the cytoplasm as a two-dimensional (2D) domain of the same dimension as the nucleoid (Fig. 1 *A*). This is an approximation based on the following considerations. In bacteria such as *E. coli*, the cytoplasm mainly occupies the space of 100–200 nm wide between the nucleoid and cell membrane. Because the free ParAs diffuse rapidly in cytoplasm (~3 $\mu m^2/s$) (45), it only takes ParA ~1–10 ms to diffuse across this short distance. Therefore, on the timescale considered (approximate seconds to minutes), the concentration profile of cytosolic ParA is uniform in the direction vertical to the nucleoid surface, which allows us to simplify the cytoplasm as a flat 2D domain, which serves as a reservoir of free ParAs. Thus, the 2D domain of cytoplasm in the model represents the effective interface of exchanging free ParAs between the cytoplasm and the nucleoid, whose dimensions was set to be the same.

To capture the dynamic changes associated with nucleoid elongation and cell growth, the model describes two effects. First, with their widths fixed at 1.0 μm, the nucleoid and cytosolic domains elongate at a constant rate (~6–18 nm/min) measured by our experiments (Fig. 1 *B*), in which we imaged HU-mCherry-tagged nucleoid over time in *E. coli* growing in minimal growth medium. The initial nucleoid length is set to be 2 μm, if not otherwise mentioned. Second, the model depicts that concurrent with nucleoid elongation, new ParA molecules are generated to keep ParA concentration constant. This captures the essence of observed autoregulation of ParA expression (46,47) and Western blot measurements showing the constant ParA concentration on population level (39).

Accordingly, the model depicts the moving boundary lengthwise and imposes hard-wall boundary condition for ParA and ParB at all edges of the simulation domain. Although ParB only localizes to the PCs (39), ParA can exchange between the nucleoid and the cytoplasm in accordance with the reaction-diffusion scheme (Fig. 1, *B* and *C*). Specifically, ParA · ATP binds to vacant, unoccupied locations of the nucleoid at a basal rate (13,48) and can transiently unbind and rebind to adjacent vacant sites via lateral diffusion (45). Upon binding to plasmid-bound ParB, the ParA · ATP no longer diffuses but forms a ParA · ATP-ParB bond, tethering the PC to the nucleoid through the nucleoid-ParA · ATP-ParB-plasmid linkage. For simplicity, we refer to the entire linkage as the ParA-ParB bond (Fig. 1 *C*).

The ParA-ParB bond formation and the subsequent deformation, similar to deforming a spring, generates a restoring force on the PC (Fig. 1 *C*). The vector sum of many individual ParA-ParB bonds across the PC collectively generates a net force that displaces the PC.

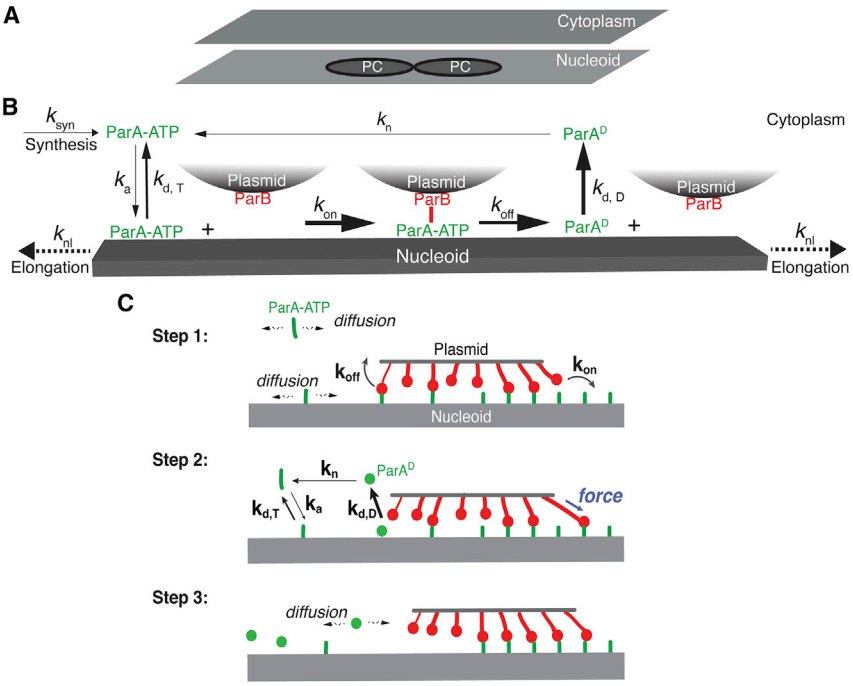

FIGURE 1 Model description. (*A*) Model setup. The model describes each PC as a circular disk and the nucleoid and the cytoplasm as the rectangular domains that share the same dimensions. (*B*) Biochemical scheme of ParAB*S* system. Briefly, ParB molecules are fixed on the PCs, whereas the ParA·ATP molecules exchange between the cytoplasm and nucleoid surface with the kinetic rates of k_a and $k_{d,\,T}$, respectively. The PC-bound ParB will rapidly bind to the local nucleoid-bound ParA·ATP at the rate of k_{on}, followed by a fast dissociation at the rate of k_{off}. The dissociation of ParA-ParB bond drives the nucleoid-bound ParA into a distinctive state, ParA^D, which rapidly turns over into the cytoplasm at the rate of $k_{d,\,D}$. At a very slow rate (k_n), the cytoplasmic ParA^D will revert into the ParA·ATP that can rebind to the nucleoid. Last, to capture the essential effects of cell growth on the ParAB*S* system, the nucleoid keeps elongating at the rate of k_{nl}, and ParA·ATP molecules are synthesized at the rate of k_{syn}. (*C*) Mechanochemical coupling of ParA-ParB bond dynamics underlies ParA gradient-based Brownian ratcheting. The Brownian ratcheting consists of three stochastic steps. Step 1: although some of the ParA-ParB bonds are dissociating, others are forming. The free ParA molecules diffuse along the nucleoid and in the cytoplasm, whereas all the ParB molecules are fixed the PC. Step 2: thermal fluctuation prestretches the forming ParA-ParB bond that pulls the PC forward. At the back of the PC, the ParA-ParB bond dissociation converts the ParA·ATP into a distinctive state (ParA^D) with a rapid turnover into the cytoplasm. Because of the slow ParA^D-to-ParA·ATP conversion, there is a time delay to replenish the local ParA·ATP on the nucleoid. This results in a ParA depletion trailing behind the PC. Step 3: the initial movement of PC creates an asymmetric local ParA concentration gradient (higher at the front, lower at the back). This breaks symmetry and drives the directed and persistent PC movement.

The movement of PC in turn changes the bond configurations. When random events (e.g., PC diffusion and stochastic ParA-ParB bond dynamics) break symmetry, the PC moves forward with the ParA-ParB bonds broken at its back (*Step 1* in Fig. 1 *C*).

We define the resulting disengaged ParA to be in a distinctive state, ParA^D (Fig. 1 *B*). Although the model does not specify whether ParA^D corresponds to an ATP-bound or ADP-bound state, it recapitulates two key aspects of disengaged ParA. First, ParA^D dissociates from the nucleoid faster than the basal turnover rate of ParA·ATP, which reflects the known effect of ParB-mediated stimulation on ParA release from the nucleoid (13,48). Second, once ParA^D dissociates into the cytoplasm, it slowly reverts to the ATP-bound state competent for DNA binding (13,48). This time delay results in a ParA-depletion zone trailing behind the moving PC, which subsequently can be refilled by cytosolic and nucleoid-associated ParA·ATP.

As the PC moves forward, the ParBs on the leading edge of the PC continue to establish new bonds with ParA·ATP on unexplored regions of the nucleoid, where the ParA·ATP concentration is higher (*Step 2* in Fig. 1 *C*). PC movement therefore maintains the asymmetric ParA concentration gradient that in turn supports further forward movement (*Step 3* in Fig. 1 *C*), resulting in a directed and persistent movement. Conceptually, our model is a 2D burnt-bridge Brownian ratchet model (49,50) in which mechanical actions of the multiple bonds not only facilitate the forward cargo movement but collectively provide tethering that quenches the cargo lateral diffusion. This drives the directed and persistent movement.

To quantitatively elucidate the proposed mechanism, we numerically computed our model with the parameters capturing in vivo conditions (Table S1). While increasing over time, the bulk-part number of ParA molecules in the nominal case was set to be approximately several thousands in the model, in accordance with the measurements (51,52). The nucleoid-bound ParA·ATPs were initially in chemical equilibrium with their cytosolic counterparts and were randomly distributed on the nucleoid, which is modeled as a rectangle domain with 5 × 5 nm square lattices of ParA·ATP-binding sites. ParBs were permanently distributed with a uniform density of ~0.013 ParB dimers/nm^2 over the PC, quantitatively reflecting the measured high propensity of ParB to spreading around the *parS* site on the plasmid (39,53–55). We modeled each ParA-ParB bond as an elastic spring. The vertical distance between the nucleoid and the PC was fixed at the equilibrium length of ParA-ParB bond (L_e). The stochastic reactions involving PC-bound ParB and nucleoid-bound and cytosolic ParAs are simulated with the kinetic Monte Carlo scheme according to the reaction scheme (Fig. 1 *B*).

The simulation workflow is as follows. At each simulation time step, each ParB can interact with available ParA·ATP within a distance L_a, and bind only one ParA at a

time with a rate of k_{on} (*Step 1* in Fig. 1 *C*). The probability of binding is proportional to $e^{-(1/2)(K_S(L-L_e)^2/k_BT)}$ for $L_a > L > L_e$; otherwise, it is 0. K_S is the spring constant of the bond, L denotes the separation between ParB and ParA·ATP. If this bond forms, L is the instantaneous bond length, and $(1/2)K_S(L-L_e)^2$ represents the associated elastic energy penalty. Importantly, given the model parameters, this energy penalty is less than the thermal energy, k_BT. Consequently, thermal energy is sufficient to prestretch the newly formed bond, which in turn provides an elastic force $\vec{f} = K_S(L-L_e)\vec{n}$ (*Step 2* in Fig. 1 *C*), where $\vec{n}$ is the unit vector of the ParA-ParB bond orientation along the tangent direction of nucleoid surface. In the simulation, we calculate the vector sum of the elastic forces from all the ParA-ParB bonds over the PC. This net force together with the PC diffusion drives PC motion for one simulation step (*Step 3* in Fig. 1 *C*), following the Langevin-like dynamics: $(k_BT/D_p)(d\vec{X}_p/dt) = \sum_i \vec{f}_i + \vec{\zeta}(t)$. Here, $\vec{X}_p$ is the centroid position of the PC, D_p is the diffusion constant of the PC, $\vec{f}_i$ is the elastic force from the ith ParA-ParB bond on the PC, and $\vec{\zeta}(t)$ represents random force resulting from thermal motion of the solvent molecules with $\vec{\zeta}(t_1)\vec{\zeta}(t_2) = (2k_BT/D_p)\delta(t_1-t_2)$, and $\delta(t_1 - t_2)$ is the Dirac δ-function.

In the next time step, the lengths and orientations of the ParA-ParB bonds are updated by the PC motion, from which the dissociation rates of the existing ParA-ParB bonds are calculated: when the bond extension exceeds the maximum, L_m (i.e., $(L - L_e) > L_m$)), the bond breaks instantaneously; otherwise, the dissociation rate is k_{off}. This dissociation reaction is next implemented in the stochastic simulation. The resulting $ParA^D$ will be released into cytoplasm and convert at a slow rate of k_n ($k_n \ll k_{off}$) to ParA·ATP. Additionally, new ParA·ATPs are generated in cytosol concurrently with the elongation of nucleoid and cytoplasmic domains at the rate of k_{nl}. These ParA·ATPs can bind to the nucleoid with a rate of k_a.

Meanwhile, PC movement from the previous time step permits PC-bound ParBs to explore new territory and form bonds with available ParA·ATPs, and vacancies on the nucleoid can be refilled by ParA·ATP rebinding from the cytosol or diffusing from adjacent sites on the nucleoid. These ParA·ATPs can establish new bonds with ParB if the PC is nearby. We then update the net force from all the ParA-ParB bonds, including changes in existing bonds and newly formed bonds. The movement of the cargo is then calculated as in the previous time step. We repeat these steps throughout the simulation over time. The simulation time step was chosen to be fixed at 10^{-4} s, which conforms to the limitation of Langevin dynamics and kinetic Monte Carlo simulations, yields consistent simulation results, and is cost effective. The model testing on the choice of time step was conducted in our previous work (29).

ParAB*S*-mediated PC partition operates near a critical point

Exploiting agent-based stochastic simulations of our model allows us to calculate the phase diagram of PC segregation motility with an elongating nucleoid (Fig. 2 *A*). It is characterized by two key control parameters, i.e., the ParA-ParB bond dissociation rate, k_{off}, and the ParA-nucleoid binding rate, k_a. In line with our previous work (32), Fig. 2 *A* shows that the replicated PCs display different motility patterns in different parameter regimes: 1) directed segregation, in which the PCs persistently move apart for a while, followed by positioning with local excursions, and 2) pole-to-pole oscillation, in which the PCs move back and forth along the nucleoid length between the two poles (Fig. S1). We note that for each point in the phase diagram, we ran stochastic simulations for $\geq$36 trajectories of 10-min dynamical evolution of the system, starting from the same initial condition and parameter set. The 10-min simulation time was chosen because 1) it is the same duration by which we extracted the PC segregation data in our experiment (see below), and 2) the simulated segregation distance at the end of the simulation has already reached the steady state so that our analysis is expected to hold up for a longer simulation time (Fig. S2). Unless otherwise mentioned, the segregation distance refers to the instantaneous distance between the two PCs at 10 min after they started to segregate. We used this PC segregation distance as a proxy to infer the partition fidelity; as suggested by our previous work (32), the more the PC segregation deviates from the half length of nucleoid, the more likely will the two PCs end up in the same half of the dividing cell, compromising the partition fidelity.

Our calculation suggested that the ParA-gradient-based Brownian ratcheting could allow the replicated PCs to undergo directed segregation and adapt their segregation distance at ~0.5 of the increasing nucleoid length (Fig. 2 *B*). This ensures the two PCs to always end up in the different cell halves, maximizing the partition fidelity. Importantly, this partition fidelity requires the ParAB*S* system to operate in a very special parameter regime (e.g., the *red dot* denoted in Fig. 2 *A*), which represents the transition of PC motility from directed segregation to pole-to-pole oscillation.

Next, we more rigorously formulated the PC partition problem in the framework of dynamical phase transition. We defined the order parameter (ψ)—which distinguishes different states of PC segregation motility—as the maximal segregation distance between the two PCs normalized by the nucleoid length within the 10-min duration. Accordingly, the average order parameter in Fig. 2 *C* is 0.56 at the transition point between directed segregation and pole-to-pole oscillation. Deviating away from this transition regime, the PCs either undergoes reduced segregation with limited excursion (e.g., the *average order parameter ~0.35* in Fig. S1 *A*) or oscillate from pole to pole (e.g., the *average*

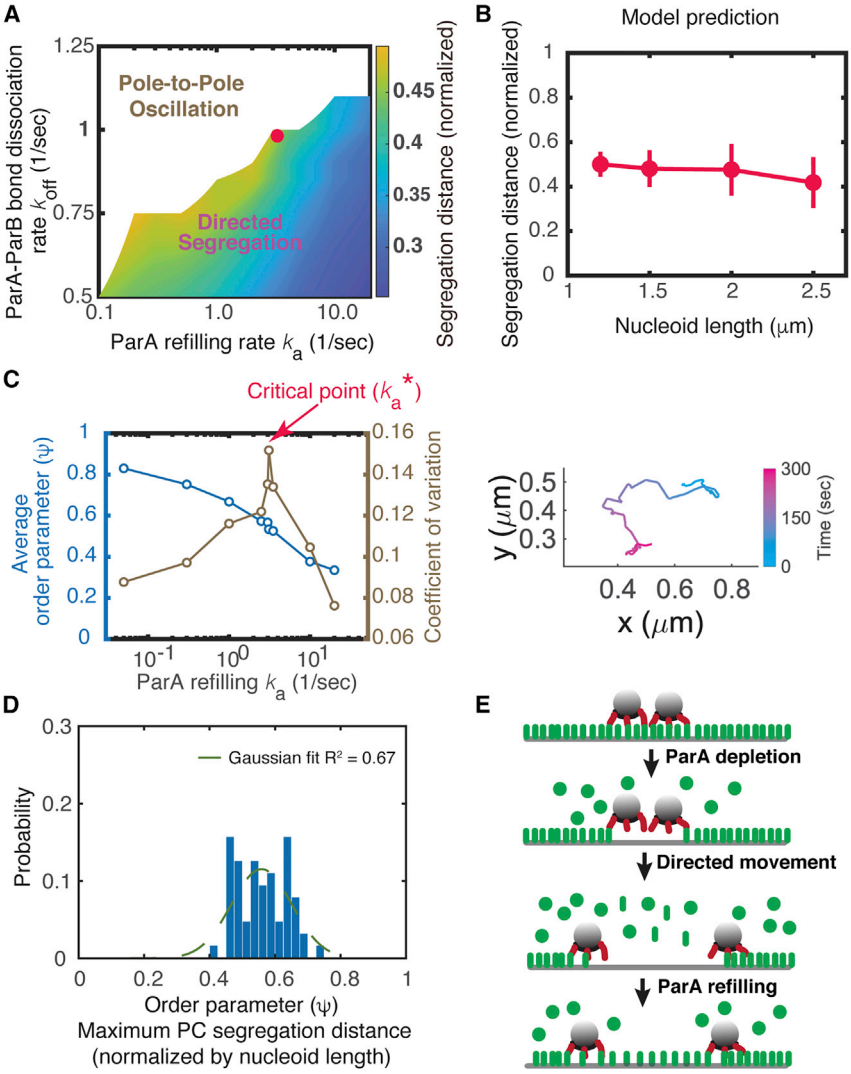

FIGURE 2 Predicted feature of near-critical-point operation of ParA-mediated PC partition. (*A*) Predicted phase diagram of PC motility controlled by (k_a and k_{off}). Here, the ParA concentration is kept constant as ~3500 molecules per micron of nucleoid length, and other parameters are kept fixed (see Table S1 for details). In our phase diagram calculation, k_{off} and k_a were varied by changing their absolute values, i.e., $k_{off} = 0.5$/s, 0.75/s, 0.85/s, 0.9/s, 1.0/s, etc., and $k_a = 0.1$/s, 0.2/s, 0.5/s, 1.0/s, 2.0/s, 2.5/s, 3.0/s, 4.0/s, etc. The log scale of k_a reflects the fact that the dependence of model result on k_a is, in general, less sensitive than k_{off}. The relative smooth phase boundary in the phase diagram reflects a balance between the quality of the figure and computational load. The red dot marks the critical point, which is further defined in (B). (*B*) Segregation distance adapts to 1/2 of the nucleoid length at the critical point in the parameter space. (*C*) Predicted characteristics of near-critical-point operation. Left: average order parameter ψ (i.e., averaged maximal segregation distance between PCs normalized by the nucleoid length over $\geq$36 trajectories of 10-min evolution) increases continuously as the ParA refilling rate decreases, whereas the variance of the order parameter peaks around the critical point (k_a^*). Note that the order parameter evolves similarly as a function of the ParA-ParB dissociation rate, k_{off}. Right: corresponding representative simulation trajectory of PC excursion with the parameter set at this critical point. (*D*) Predicted statistical distribution of order parameter ψ at the critical point ($n = 64$). (*E*) Schematic illustration of the physical nature of near-critical-point partitioning. For (*A*) and (*B*), the segregation distance refers to the instantaneous distance between the two PCs at 10 min after they started to segregate.

order parameter ~0.85 in Fig. S1 *B*). Either way, the variations of their order parameter distribution are very narrow (Fig. S1, *A* and *B*). In contrast, at this particular parameter set, the PCs are predicted to undergo directed segregation but with extensive excursions (the *right panel* in Fig. 2 *C*). More importantly, the corresponding statistical distribution of ψ is very broad and non-Gaussian (Fig. 2 *D*), and the correlation length between the PC movements peaks (~420 nm) (Fig. S3 *A*). Together, these general features are akin to the signatures of critical dynamics (56). We note that, technically, the concept of critical point in statistical physics only applies to infinite-large systems. With our finite-size system here, we used the term of critical point in a broader sense. With this perspective, the PC partition is predicted to operate at a critical point.

To test the prediction, we conducted time-lapse epifluorescence microscopy experiments using the well-established F-plasmid partition system in *E. coli* (10,38). The F plasmid is present at approximately two copies per chromosome per cell (57). We used functional fluorescent fusion proteins $ParB_F$-mTq2 (38) and HU-mCherry to label the mini-F plasmid and the nucleoid, respectively (Fig. 3 *A*). *E. coli* cells were grown in two different conditions, giving rise to two generation times of 45 and 242 min with an average mini-F copy number per cell of 3.6 and 2.8, respectively (see Table 1). In these two conditions, we found that cells displayed 3.1 and 2.2 fluorescent foci per cell, respectively, indicating that during most of the cell cycle, plasmids are not clustered.

Then, we measured the nucleoid size along the long cell axis and the distance between two PCs in two-foci cells, in which we imaged the PC partitioning process for 10 min after the two PCs started to segregate. Our data showed that the PC segregation distance (at the 10-min time point) adapts to half of the nucleoid length independently of the growth condition as the nucleoid increased from 1.2 to 3.0 microns (Fig. 3 *B*). Critically, the PCs indeed undergo extensive excursion (Fig. 3 *C*). The order parameter

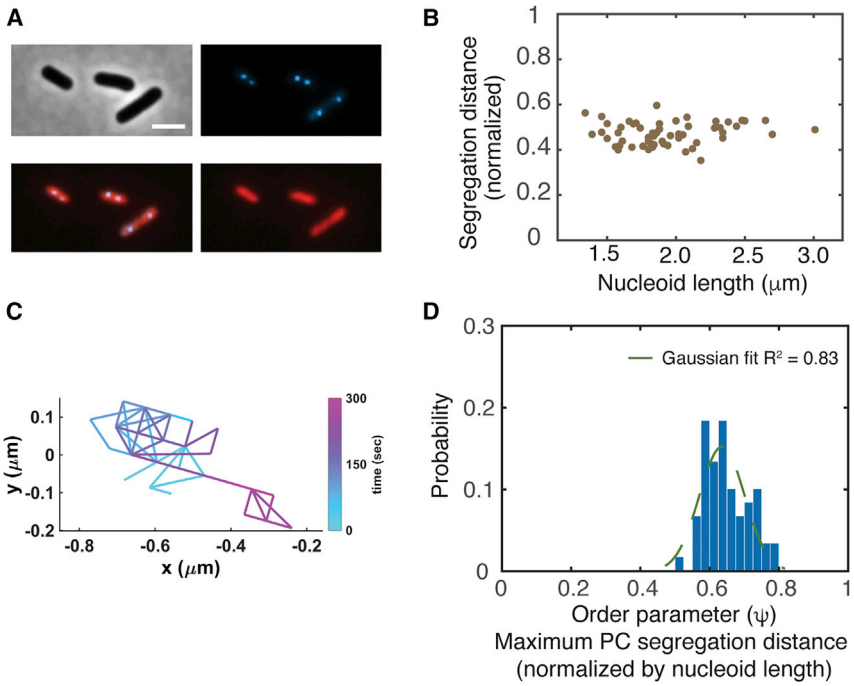

FIGURE 3 Near-critical-point operation of ParA-mediated PC partition. (*A*) Experimental setup of two-color live-cell imaging of F plasmids in wild-type *E. coli*. Cells are observed in phase contrast (*top left*) and in the blue (*top right*) and red (*bottom right*) channels for fluorescence microcopy to observe $ParB_F$-mTq2 or $ParA_F$-mVenus, respectively. Shown is the overlay of blue and red channel (*bottom left*). Scale bars, 2 μm. (*B*) Experimental data demonstrate that PC segregation distance adapts to 1/2 of the nucleoid lengths ($n = 58$). Data from cells grown at 30°C in MGly with or without casamino acids were represented on the same graph because they display the same trend. The segregation distance refers to the instantaneous distance between the two PCs at 10 min after they started to segregate. (*C*) A representative saltatory trajectory of PC excursion. (*D*) Non-Gaussian distribution of order parameter ψ (i.e., the maximal PC segregation distance of PC normalized by the nucleoid length within 10-min duration) ($n = 60$).

(ψ)—defined as the maximal segregation distance normalized by the nucleoid length during the 10 min—displays a broad distribution with the average of 0.65 (Fig. 3 *D*). This is akin to the predicted case at the critical point (Fig. 2, *C* and *D*). Additionally, the correlation length of the PC movements is measured to be ∼500 nm (Fig. S3 *B*), similar to the predicted value (∼420 nm) (Fig. S3 *A*). In contrast, our data are distinct from the predicted cases that deviate away from the critical point (Fig. S1), in which not only the distribution of order parameter ψ is much narrower, but their averages are either too small (∼0.35) or too large (∼0.85). To more rigorously gauge whether and how our results differ from a Gaussian distribution, we resorted to two statistical measures. First, we calculated the excess kurtosis value, which is 0 for the perfect Gaussian and −1.2 for the uniform distributions. The excess kurtosis value is −0.75 for our experimental data and −1.0 for the model result (Figs. 2 *D* and 3 *D*, respectively). Second, we calculated the χ^2-value between the cumulative distribution functions of our data and Gaussian distribution. The χ^2-value is 0 for the perfect Gaussian: the larger it is, the more the result deviates from Gaussian distributions. With this measure, the χ^2-value is 8.9 for our experimental data and 6.6 for our model result (Figs. 2 *D* and 3 *D*, respectively). Together, the order parameter of our PC segregation data has the average of 0.65 with a broad distribution that saliently deviates from a Gaussian distribution, supporting the prediction that the PC partition operates at a critical point (Fig. 2 *D*).

We interpret the physical nature of this near-critical-point PC partition as follows (Fig. 2 *E*): replicated PCs undergoes directed segregation because of their initial side-by-side

TABLE 1 High fidelity of F-plasmid partition in *E. coli*

	Loss rate[a]		Copy number[b]			
Generation time[c] T (min)	pJYB249	pDAG115	At cell division (*n*)	Per cell (*cn*)	Average foci number per cell[d] (*fn*)	Clusterization ratio[e]
45	<0.001	0.058 ± 0.1	5.16	3.57	3.13	0.12
242	0.001	0.128 ± 0.002	4.06	2.81	2.18	0.22

The level of plasmid F clusterization is low in fast and slow *E. coli* growing conditions. The clusterization level is estimated by the difference between the average number of foci and the average number of plasmids per cell.

[a]The loss rate of the plasmids used in the microscopy assay (pJYB249) and in the determination of the plasmid copy number (pDAG115) were obtained from at least three independent measurements, except for pJYB249 grown in the presence of CSA performed in duplicate. pDAG115 is a partition defective mini-F plasmid (41) that allows for estimating the copy number at cell division (see Materials and methods).

[b]The plasmid copy number per cell is ln2 times the copy number at cell division *n* (19).

[c]The generation time (T) was estimated from measurements of culture optical densities at 600 nm.

[d]The number of foci per cell was determined by epifluorescence microscopy.

[e]The clusterization ratio is determined by the following formula: $(cn - fn)/cn$.

arrangement. As they deplete the ParA underneath from the nucleoid, the local nucleoid-bound ParA concentration field becomes asymmetric for each PC, which sets the directed movement. As the PCs move apart, each PC associates with a ParA-depletion zone, like "a sphere of influence." It takes some time for the depleted ParAs to rebind the nucleoid, which eventually re-establish the symmetric ParA distribution surrounding each of the PCs, thus positioning the PCs. As such, the ParA-ParB bond dissociation confers the PC directed segregation, whereas ParA refilling event hinders it. The balance between these two activities defines the critical point. At this critical point, the PC's ParA-depletion zones (or spheres of influence) overlap with a linear dimension comparable with the nucleoid length, the essence of which is qualitatively captured by the long correlation length between PC movements (Fig. S3). This allows the PCs to feel not only the presence of each other but the boundary of the elongating nucleoid.

Together, our results suggest that although the ParA-ParB interaction is local, operation of ParA gradient-based Brownian ratchet mechanism—near a critical point—can provide the PCs a global view, allowing sensitive adaptation of their segregation distance to the increasing nucleoid length. That is, the near-critical-point operation allows ParA-mediated partition machinery to measure the cellular distance by molecular interactions.

ParAB*S*-mediated PC partition is robust against cell-to-cell ParA level variations

Given the sensitive nature of partitioning near a critical point, the next question is as follows: how does the ParAB*S*-mediated partition manage to buffer against fluctuations inside cells, a central topic of control for any biological systems? We are attracted to the view that the control parameters of a cell are hard-wired genetically—shaped by the long evolutionary process—to a critical point that is biologically most advantageous for survival and proliferation (58). In light of this, genome partition is a subprocess enslaved to the entire cell dynamics; the robustness of genome partition specifically refers to how well it copes with the uncertainties originated from outside of the cell or from other parts of the intracellular dynamics.

To begin to characterize the cellular fluctuations relevant to ParAB*S*-mediated partition, we measured the intracellular ParA concentration by coupling ParA to mVenus fluorescent peptide ($ParA_F$-mVenus) in cells, allowing the detection of the nucleoid length and PC positioning (as above). The data showed that [ParA] varies from cell to cell over 10-fold in wild-type *E. coli* (Fig. 4 *A*). Despite the large variations of [ParA], the PC partition still adapts the separation distance to ~0.5 of various nucleoid lengths (Fig. 4 *A*), ensuring the high partition fidelity observed with a plasmid loss rate $\leq 0.1\%$ (see Table 1).

To understand the robustness measure adopted by the PC partition system, we reasoned that both the ParA-ParB dissociation rate, k_{off}, and the ParA-nucleoid binding rate, k_a, might change with the [ParA]. This way, the partition could still operate near the critical point when [ParA] varies, i.e., rather than at a fixed point in the parameter space in Fig. 2 *A*, the partition operates along the transition line between the states of pole-to-pole oscillation and directed segregation. To explore this possibility, we tried to measure the $ParA_F$-$ParB_F$ dissociation rate k_{off} by monitoring the PC foci segregation rates. According to our model, the PC segregation speed is proportional to the $ParA_F$-$ParB_F$ bond dissociation rate (32). Our data show that the PC segregation speed, although varying somewhat, is insensitive to the [ParA] (Fig. 4 *B*).

As demonstrated by our previous modeling result (32), the speed of directed segregation equals to the ParA-ParB bond dissociation rate (k_{off}) times a constant characteristic of individual ParA-ParB bond length. Given the experimental data in Fig. 4 *B* showing that the segregation speed is insensitive to the variation in ParA intensity, this suggests that the ParA-ParB bond dissociation rate (k_{off}) is insensitive to the variation in ParA intensity. We reasoned that because the partition machinery operates at a critical point in the parameter space (k_a* and k_{off}*), as demonstrated in Figs. 2 and 3, the fixed k_{off}* means that the k_a* is insensitive to the [ParA] variation in our system. We are therefore attracted to the idea that both k_a* and k_{off}* remain insensitive to the [ParA] variation. Following this line of argument, our simulation showed that with the fixed k_a* and k_{off}*, the segregation distance in the model decreases sharply as [ParA] increases (Fig. 4 *C*), inconsistent with the observations (Fig. 4 *B*). This discrepancy suggests the partition

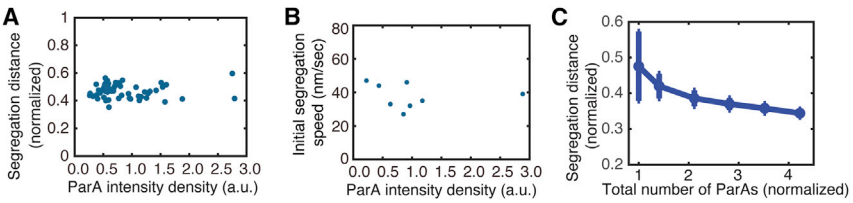

FIGURE 4 Robustness of PC partition against variations of ParA level. (*A*) Experimental data showing the PC segregation distance normalized by the nucleoid length is insensitive to the large cell-to-cell ParA level fluctuations ($n = 58$). (*B*) Initial segregation speed is insensitive to the ParA level. (*C*) This model cannot buffer the near-critical-point partition against ParA level fluctuations. For (*A*) and (*C*), the segregation distance refers to the instantaneous distance between the two PCs at 10 min after they started to segregate.

robustness entails additional factor(s) and thus precipitates the question of what buffers the robustness of PC segregation against [ParA] variations.

PC-mediated ParA localization underlies partition robustness against bulk [ParA] variations

Based on in vitro and in vivo data suggesting that ParA could bind to the plasmid through its interaction with ParB and nonspecific DNA (11,13,16), our leading hypothesis is that the intracellular ParA could localize around the PC and create a local environment that buffers the partitioning against the bulk [ParA] variation (Fig. 5 *A*). To test the hypothesis, we first extended the in vivo model to incorporate this PC-mediated ParA localization effect. We assumed the cytosolic ParA to have a high binding affinity to PC but with a transient lifetime before turning over into cytoplasm (Fig. 5 *A*), characterized by the $k_{a,\ plasmid}$ and $k_{d,\ plasmid}$ rates. Because of the finite size of the PC, the model imposed an upper limit in the number of ParA molecules, approximately hundreds that simultaneously localize to the PC. This saturation level is based on the in vitro measurements (13,31). We further assumed that right after releasing from the PC, the ParA has a reduced propensity to bind to the nucleoid. This last assumption is based on the observation that the interaction with ParB not only speeds up the dissociation of ParA from nucleoid but inhibits the ParA-nucleoid binding (13). Below, we will present the typical model result. Additional model investigations on how the PC-mediated ParA localization effects influence the fidelity of PC partition are presented in Fig. S4, which shows that the essential features in Fig. 5 persists in a broad range of parameter space.

Equipped with this ParA localization effect, simulating this integrated mathematical model shows that it preserves the key features of near-critical-point operation (Fig. S5, *A* and *B*) and especially the sensitive adaptation of PC segregation distance to the nucleoid lengths (Fig. S5 *C*). More importantly, these PC-localization effects of ParA could simultaneously explain the robustness of partitioning evidenced in *E. coli.* (Fig. 4 *A*). That is, the segregation of the replicated PCs by the half of the nucleoid length remains largely insensitive to the [ParA] variations (Figs. 5 *B* and S5 *C*). Such a buffering effect entails an appropriate ParA accumulation around the PC (Fig. 5 *C*). When the on rate ($k_{a,\ plasmid}$) is too slow, the PC not only depletes the ParA from underneath but cannot supply enough ParA to refill the depletion zone underneath so that the PC becomes diffusive (the *lower portion* of Fig. 5 *C*). When the on rate is too fast and the off rate is too slow, the PC will accumulate too many ParAs so that the nucleoid-bound ParA will become very sparse, likewise favoring diffusive movement (the *upper left corner* of Fig. 5 *C*). However, as the off rate increases while keeping the on rate very fast, the PC will funnel the cytoplasmic ParA to the local nucleoid at very high concentration. This significantly increases the overall ParA binding to nucleoid, immobilizing the PCs (the *upper right corner* of Fig. 5 *C*). In these extreme limits, the partition system loses its robustness of adapting the PC segregation distance to the half of an elongating nucleoid (Fig. 5 *C*). To ensure the PC partition fidelity, the ParA thus is expected to localize around the PCs with only severalfold accumulation at its peak concentration.

To begin to test this prediction, we resorted to live-cell imaging to discern whether and how ParA accumulates around the PC. To better resolve the subcellular pattern,

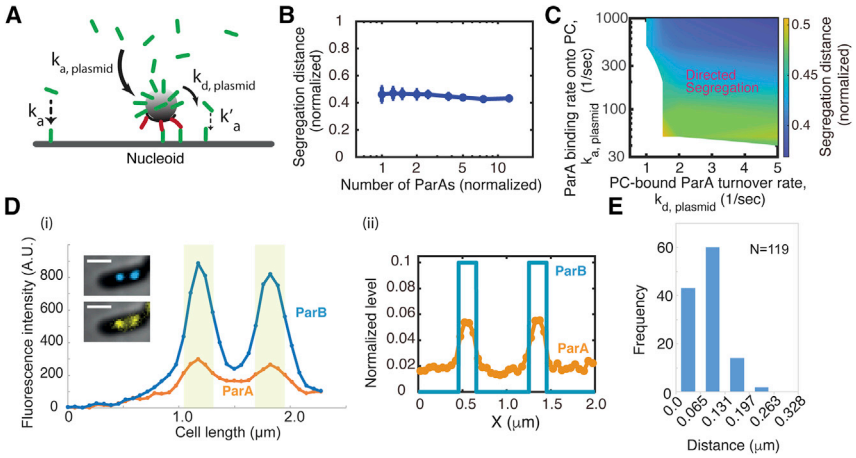

FIGURE 5 PC localization of ParA explains the partition robustness. (*A*) Model scheme of PC-mediated ParA localization. The red rod represents the PC-bound ParB, and green rod the ParA. The arrows denote the conversion reaction, wherein the thicker the arrow is, the faster is the reaction. The dotted arrow represents the relatively slow reaction that a cytosolic ParA bind to nucleoid. (*B*) The amended model can ensure the fidelity of near-critical-point partition against the ParA level fluctuations. Note, the same parameter set here also simultaneously ensures the sensitive adaptation of segregation distance to nucleoid lengths (see Fig. S5 *C*). (*C*) Predicted phase diagram of the dependence of PC partition fidelity on the ParA localization effects. For each point in the phase diagram, we ran stochastic simulations for ≥36 trajectories of the 10-min dynamical evolution of the system, starting from the same initial condition and parameter set. The segregation distance reports the average value of ≥36 trajectories at the end of the simulation. (*D*) Representative spatial profiles of ParA and PC along the cell length. (*i*) Live-cell experimental result. Line scan analysis of the fluorescence intensities in arbitrary units along cell length. Blue and orange lines correspond to the blue ($ParB_F$-mTq2) and yellow ($ParA_F$-mVenus) channels, respectively. The corresponding cell images is displayed in the graph. Scale bars, 1 μm. The gray area corresponds to four pixels (262 nm) around the PC peak. (*ii*) Model result. (*E*) Histogram of PC-ParA colocalization. For (*B*) and (*C*), the segregation distance refers to the instantaneous distance between the two PCs at 10 min after they started to segregate.

we sought the experimental conditions that have a low amount of ParA without perturbing other key factors of the system. We took the advantage of our observation that in wild-type cells, ParA distributes asymmetrically between the two daughter cells at cell division (Fig. S6 *A*), which not only underlies the large cell-to-cell variation of [ParA] (Fig. 4 *A*) but presents a natural testing ground of our model. We thus focused our analyses on the newborn cells that have inherited a low amount of $ParA_F$-mVenus (Fig. S6 *A*), which allows for a better detection of localized signals. In these cells with low intracellular amount of ParA, we also imaged the PC locations with $ParB_F$-mTq2 that form intense foci. We measured the peak intensity along the cell length for both ParA and ParB by applying a line scan analysis. Although ParA-mVenus displays faint foci, they appeared very close to PCs; importantly, they did not result from cross-fluorescence imaging (Fig. S6 *B*). Fig. 5 *Di* presents a representative measurement, and Fig. S6 *C* provides more detailed analysis. Briefly, in the 58 cells analyzed, we observed that the vast majority of them (41 cells) display the same number of ParA and ParB foci, 14 cells display one more ParA focus than ParB, and three cells have one more ParB focus than ParA. However, we could not accurately measure the ParA intensity accumulation around PC because of 1) the cell-to-cell variation in [ParA], and 2) the depletion of ParA provoked by ParB. Nevertheless, the observation of discrete ParA patches indicates that ParA accumulates several-fold compared with the intracellular level in the close vicinity of PCs, consistent with our predictions (Fig. 5 *Dii*). To further quantify the degree of colocalization of the ParA and ParB foci, we measured the distance between the peak intensities for each pair of ParA and ParB foci ($n = 119$; Fig. 5 *E*). We found that for 98% of the pairs, the ParA and ParB peak intensities are within two pixels (131 nm). Given the 200–250-nm resolution of epifluorescence microscopy due to the light diffraction limit, our data show that ParA and ParB foci are highly colocalized, providing strong support to the predicted PC-ParA colocalization. Importantly, regardless of the ParA levels (Figs. 4 and S6), the corresponding PC segregation distance always adapts to approximately half of the nucleoid length (Fig. 3 *A*) with a very low error rate of the partitioning (<0.1%) (see Table 1). Combining our model and experimental data, we suggest that PC-mediated ParA localization underlies the fidelity of PC partitioning against [ParA] variations.

DISCUSSION

In this study, we provided direct evidence—with a mechanistic underpinning—that the partitioning of low-copy-number plasmids operates near a critical point. The near-critical-point operation allows the partition machinery to gauge the size of the entire nucleoid and, accordingly, adapt the plasmid segregation distance to the half length of the elongating nucleoid (Fig. 3). Segregating by half of the nucleoid length renders that each cell half always inherits at least one PC, ensuring the partition fidelity, which is also observed in other ParAB*S* systems (e.g., (59)). We further provided the data suggesting that the PC localizes cytoplasmic ParA to its neighborhood. This spatial control creates a local environment that buffers the near-critical-point partition against the fluctuations in bulk [ParA] (Fig. 5), which allows the cell to manage the dichotomy of sensitive adaptation and robust execution of low-copy-number plasmid partitioning. This way, each PC defines its own sphere of power that allows the PC to "self-drive" by generating the path ahead and erasing the trail behind.

This model predicts ParA-PC-localization effects by only focusing on the simplest biochemical scheme. Nonetheless, we indeed observed the ParA-PC localization when the ParA level is low in wild-type cells (Fig. 5, *D* and *E*). Given that 1) PC is much smaller in size than the nucleoid, and 2) it competes with the nucleoid to bind the same pool of cytoplasmic ParA, this observation indicates that ParA-PC binding affinity must be much higher than its nucleoid-counterpart. Because ParA binds to nonspecific DNA, without preference for plasmid over chromosome DNA, its colocalization with PC is expected to arise from its interactions with the PC-bound ParB. This notion is consistent with the extensive experimental evidence that the PC-bound ParB interacts with the cytoplasmic ParA (60–62). We thus expect ParA to localize around the PC when its level increases in wild-type cells, although it would be difficult to experimentally discern its localization pattern with a high background. Importantly, according to our model (Fig. 5, *B* and *C*), this PC localization of ParA ensures the fidelity of PC partition regardless of the ParA level variations that naturally occur in wild-type cells (Fig. 4 *A*; Table 1).

The direct testing of how the PC-localized ParA drives the partition fidelity of the *parS*-carrying DNA is not simple. Point mutations that disrupt ParA-ParB interactions and compromise ParA ATPase activity were identified, e.g., $ParA_F$-K120Q and $ParA_F$-K120R (63). These mutations that drastically changed the spatial profile of $ParA_F$ from foci (Fig. 5 *D*) to uniform distribution along the nucleoid (64) were reported to increase the loss rate of the F plasmids by 400–800-fold (63). These observations would be consistent with the model proposal that decreasing the PC localization of ParA compromises the partition fidelity (i.e., the *lower left corner* of Fig. 5 *C*). We caution, however, that the point mutations render the PC to lose contact with the nucleoid and, hence, the active partition after all (34). It is possible that localizing to PC is integral of ParA's normal activities. Thus, identifying a ParA variant that is specifically perturbed in its PC localization but not in other activities essential to partition is not easily accessible. Such a study is also be complicated with the transient interactions between ParA and ParB that both exist in different biochemical states (13,48,65). The recent findings that ParB binds CTP (62,66,67) and that *parS*-mediated CTP hydrolysis

stimulates ParA interaction (62,67) could open interesting molecular clues to control this interaction.

Moreover, our model describes the PC partitioning along the nucleoid surface as a 2D problem. Recent experiments, however, suggest that the PC may move inside the nucleoid (34). Let us consider the simplest three-dimensional (3D) case first, followed by more complex scenarios. The simplest 3D scenario is that the interactions between the PC-bound ParB and nucleoid-bound ParA are still along the surface of the PC and the nucleoid should have the void space that allows the PC to move through. In this scenario, the PC moving through the nucleoid is like a sphere moving through a hollow cylinder. Now, unfolding the hollow cylinder will render a flat substrate, akin to our 2D model. Within this simplest 3D case, the 3D effects could alter several key parameters of this model. First, trapping inside the nucleoid likely slows down the diffusion of the PC. Second, the number of ParA-ParB bonds in 3D might be different from its 2D counterpart because some ParB buried within the PC may not be available for bond formation with the nucleoid-bound ParA. Third, the nucleoid DNA density, instead of being uniform, is reported to have high- and low-density regions (34). In this regard, our phase diagram studies show that the essence of our conclusion—i.e., the nature of critical-point-operation of PC partition and the effect of PC localization of ParA on the robustness against [ParA] variations—is largely preserved against variations of these relevant model parameters (Fig. S7).

We note that a more realistic 3D model may contain many factors that are currently not well characterized. For instance, we do not know the interior landscape of the nucleoid or whether and how the nucleoid DNA changes its conformation to accommodate the PC movement. Additionally, instead of acting as impenetrable structures, the PC and nucleoid could be amorphous so that ParA and ParB are able to freely enter and exit, offering a more complex interaction network that remains to be explored. Given these uncertainties, we will leave the 3D model to our future study.

Likewise, the self-drive of our Brownian ratcheting consists of a persistent "driving" followed by the positioning during directed segregation. Conceptually, this is akin to a positive feedback followed by a delayed negative feedback in stochastic biochemical network, the temporal dynamics of which can give rise to bi-stability and checkpoint (68). However, our system plays out not only in time but in space; it is an open question of whether and how this self-drive of our system involves the ingredients of bi-stability and checkpoint. Our future study will explore how the PC-mediated ParA localization influences the mathematical structure of spatial-temporal feedbacks in our system.

Furthermore, this PC-mediated ParA localization effect has its own limitation in ensuring the partition fidelity (Fig. S8 *A*). When the nucleoid becomes too long, this model would predict the partition machinery to lose its ability of adapting the segregation distance to half of the nucleoid length. Interestingly, as the nucleoid gets longer, the low-copy-number plasmids are reported to replicate accordingly to keep the plasmid/chromosome ratio constant. The latter events increase the number of PC foci. This way, each PC focus "commands" a unitary length of nucleoid as its power of sphere, resulting in the following equidistant pattern (22,69): the two PCs on the same nucleoid segregate by 1/2 of the nucleoid length, whereas the three PCs will segregate by ∼1/3 of that nucleoid length and so on. A size scaling emerges between the PC interdistance and the nucleoid length as a function of PC foci numbers. Although the notations of size scaling and size control have been indicated in biological systems (70–74), our work here provides a functional perspective in a way similar to spindle-cell size scaling (75).

Conversely, the spatial control over near-critical-point operation defines an optimal PC size that maximizes the upper limit of nucleoid length that the PC partitioning can adapt its segregation distance (Fig. S8 *B*). This is because PC size directly determines how many ParA-ParB bonds can be formed: if the PC is too small, then there will be too few ParA-ParB bonds to quench the diffusive motions and drive the directed PC movement. On the other hand, if the PC is too large, then it will yield too many ParA-ParB bonds so that the PC will get anchored for a long time, preventing movement. Consistent with this view, the optimal PC size can be modulated by the biochemical kinetics of ParA-ParB interactions (e.g., the off rate of ParA-ParB bond), which operates near the critical point. For instance, the faster the off rate, the larger the optimal PC size becomes (Fig. S8 *C*). For the given parameter set in Fig. S8 *C*, the optimal PC size is predicted to range between ∼62 and 130 nm. Because the PC is modeled as a 2D circular disk here, the predicted PC size should correspond to a 3D sphere with half its size, if we assume that they share the same surface area and, hence, the same number of ParA-ParB bonds. In this sense, the predicted optimal PC size in 3D would be ∼31–65 nm. Strikingly, this is consistent with the PC size of 43 ± 7 nm measured in vivo by super-resolution microscopy (38). In the light of partition fidelity, our results here provide a functional viewpoint of PC size regulation: 1) PC size may be optimized for the maximal ability of adapting PC partition to the nucleoid length, and 2) this optimal PC size can vary from system to system, depending on the kinetics of ParA partition machinery. In a bigger picture, although PC localizes the ParA, as demonstrated in this study, the ParA may reciprocally regulate the PC size (38), both of which contribute to the fidelity of PC partition. These findings bring up an interesting question of exactly how this feedback between ParA-mediated PC size regulation and PC-mediated ParA localization shapes the PC formation and the subsequent partitioning processes, which we will study in the near future.

Lastly, because low-copy-number plasmids provide selective advantages for bacterial survival, connecting the

physical mechanism with the fidelity of DNA partition could allow us to understand how evolution might shape the near-critical-point behavior of a biological process to maximize its function. Interestingly, although widely conserved in both genome segregation (i.e., plasmids and chromosomes) and subcellular organelle trafficking in bacteria (76,77), the ParAB*S*-mediated partitioning displays distinct spatial-temporal features in these different systems (12,78–80). With these diverse spatial-temporal dynamics, our work provides a starting point to shed light on how the near-critical-point operation of the same machinery adapts to different systems with different sizes and geometries. In a broader context, reaction-diffusion processes of molecular systems were proposed to function as a ruler to measure the cellular distances in bacteria (e.g., the dynamics of the Min-CDE system facilitates the determination of cell division site (81–83) or the intracellular machinery controls the flagellum length (84,85)). In general, the reaction and diffusion parameters need to be fine-tuned to achieve this length control and sensing. It remains unknown whether these systems operate near a critical point and how they ensure the robust measurement of cellular distance against noises. We suggest that the principles of spatial controls over the near-critical-point operation provide a possible solution to this fundamental question of cell biology: how do cells faithfully measure cellular-scale distances by only using molecular-scale interactions? We will investigate along this direction in the future.

SUPPORTING MATERIAL

Supporting material can be found online at https://doi.org/10.1016/j.bpj.2021.08.022.

AUTHOR CONTRIBUTIONS

J.-Y.B. and J.L. designed the research project. L.H. and J.R. performed the model computation and experimental testing, respectively. L.H., J.R., J.-Y.B., and J.L. analyzed the data and wrote the manuscript.

ACKNOWLEDGMENTS

The authors thank Drs. Anthony Vecchiarelli for the inspiring critiques of the work and Christian Rouvière (ImageAnalysis, Centre de Biologie Intégrative) for implementing a python-based analysis tool for colocalization measurements.

L.H. and J.L. are supported by Johns Hopkins University Startup Funds and Catalyst Awards and National Science Foundation grant 2105837. J.R. and J.-Y.B. are supported by an entre National de la Recherche Scientifique 80Prime grant.

REFERENCES

1. Mora, T., and W. Bialek. 2011. Are biological systems poised at criticality? *J. Stat. Phys.* 144:268–302.
2. Hesse, J., and T. Gross. 2014. Self-organized criticality as a fundamental property of neural systems. *Front. Syst. Neurosci.* 8:166.
3. Krotov, D., J. O. Dubuis, …, W. Bialek. 2014. Morphogenesis at criticality. *Proc. Natl. Acad. Sci. USA.* 111:3683–3688.
4. Mojtahedi, M., A. Skupin, …, S. Huang. 2016. Cell fate decision as high-dimensional critical state transition. *PLoS Biol.* 14:e2000640.
5. Tetzlaff, C., S. Okujeni, …, M. Butz. 2010. Self-organized criticality in developing neuronal networks. *PLoS Comput. Biol.* 6:e1001013.
6. Elowitz, M. B., A. J. Levine, …, P. S. Swain. 2002. Stochastic gene expression in a single cell. *Science.* 297:1183–1186.
7. Kaern, M., T. C. Elston, …, J. J. Collins. 2005. Stochasticity in gene expression: from theories to phenotypes. *Nat. Rev. Genet.* 6:451–464.
8. Newman, J. R. S., S. Ghaemmaghami, …, J. S. Weissman. 2006. Single-cell proteomic analysis of *S. cerevisiae* reveals the architecture of biological noise. *Nature.* 441:840–846.
9. Nordström, K., and S. J. Austin. 1989. Mechanisms that contribute to the stable segregation of plasmids. *Annu. Rev. Genet.* 23:37–69.
10. Bouet, J.-Y., and B. E. Funnell. 2019. Plasmid localization and partition in *Enterobacteriaceae*. *Ecosal Plus.* 8:1–23.
11. Hatano, T., and H. Niki. 2010. Partitioning of P1 plasmids by gradual distribution of the ATPase ParA. *Mol. Microbiol.* 78:1182–1198.
12. Lim, H. C., I. V. Surovtsev, …, C. Jacobs-Wagner. 2014. Evidence for a DNA-relay mechanism in ParABS-mediated chromosome segregation. *eLife.* 3:e02758.
13. Vecchiarelli, A. G., L. C. Hwang, and K. Mizuuchi. 2013. Cell-free study of F plasmid partition provides evidence for cargo transport by a diffusion-ratchet mechanism. *Proc. Natl. Acad. Sci. USA.* 110:E1390–E1397.
14. Vecchiarelli, A. G., K. C. Neuman, and K. Mizuuchi. 2014. A propagating ATPase gradient drives transport of surface-confined cellular cargo. *Proc. Natl. Acad. Sci. USA.* 111:4880–4885.
15. Jacob, F., S. Brenner, and F. Cuzin. 1963. On the regulation of DNA replication in bacteria. *Cold Spring Harb. Symp. Quant. Biol.* 28:329–348.
16. Bouet, J.-Y., Y. Ah-Seng, …, D. Lane. 2007. Polymerization of SopA partition ATPase: regulation by DNA binding and SopB. *Mol. Microbiol.* 63:468–481.
17. Leonard, T. A., P. J. Butler, and J. Löwe. 2005. Bacterial chromosome segregation: structure and DNA binding of the Soj dimer–a conserved biological switch. *EMBO J.* 24:270–282.
18. Ah-Seng, Y., J. Rech, …, J.-Y. Bouet. 2013. Defining the role of ATP hydrolysis in mitotic segregation of bacterial plasmids. *PLoS Genet.* 9:e1003956.
19. Gordon, S., J. Rech, …, A. Wright. 2004. Kinetics of plasmid segregation in *Escherichia coli*. *Mol. Microbiol.* 51:461–469.
20. Niki, H., and S. Hiraga. 1997. Subcellular distribution of actively partitioning F plasmid during the cell division cycle in *E. coli*. *Cell.* 90:951–957.
21. Ringgaard, S., J. van Zon, …, K. Gerdes. 2009. Movement and equipositioning of plasmids by ParA filament disassembly. *Proc. Natl. Acad. Sci. USA.* 106:19369–19374.
22. Sengupta, M., H. J. Nielsen, …, S. Austin. 2010. P1 plasmid segregation: accurate redistribution by dynamic plasmid pairing and separation. *J. Bacteriol.* 192:1175–1183.
23. Walter, J. C., J. Dorignac, …, F. Geniet. 2017. Surfing on protein waves: proteophoresis as a mechanism for bacterial genome partitioning. *Phys. Rev. Lett.* 119:028101.
24. Eliasson, A., R. Bernander, and K. Nordström. 1996. Random initiation of replication of plasmids P1 and F (oriS) when integrated into the *Escherichia coli* chromosome. *Mol. Microbiol.* 20:1025–1032.
25. Helmstetter, C. E., M. Thornton, …, J. E. Grimwade. 1997. Replication and segregation of a miniF plasmid during the division cycle of *Escherichia coli*. *J. Bacteriol.* 179:1393–1399.

26. Onogi, T., T. Miki, and S. Hiraga. 2002. Behavior of sister copies of mini-F plasmid after synchronized plasmid replication in *Escherichia coli* cells. *J. Bacteriol.* 184:3142–3145.

27. Niki, H., and S. Hiraga. 1999. Subcellular localization of plasmids containing the oriC region of the *Escherichia coli* chromosome, with or without the sopABC partitioning system. *Mol. Microbiol.* 34:498–503.

28. Bakshi, S., H. Choi, …, J. C. Weisshaar. 2014. Nonperturbative imaging of nucleoid morphology in live bacterial cells during an antimicrobial peptide attack. *Appl. Environ. Microbiol.* 80:4977–4986.

29. Hu, L., A. G. Vecchiarelli, …, J. Liu. 2015. Directed and persistent movement arises from mechanochemistry of the ParA/ParB system. *Proc. Natl. Acad. Sci. USA.* 112:E7055–E7064.

30. Hu, L., A. G. Vecchiarelli, …, J. Liu. 2017. Brownian ratchet mechanisms of ParA-mediated partitioning. *Plasmid.* 92:12–16.

31. Hwang, L. C., A. G. Vecchiarelli, …, K. Mizuuchi. 2013. ParA-mediated plasmid partition driven by protein pattern self-organization. *EMBO J.* 32:1238–1249.

32. Hu, L., A. G. Vecchiarelli, …, J. Liu. 2017. Brownian ratchet mechanism for faithful segregation of low-copy-number plasmids. *Biophys. J.* 112:1489–1502.

33. Debaugny, R. E., A. Sanchez, …, J.-Y. Bouet. 2018. A conserved mechanism drives partition complex assembly on bacterial chromosomes and plasmids. *Mol. Syst. Biol.* 14:e8516.

34. Le Gall, A., D. I. Cattoni, …, M. Nollmann. 2016. Bacterial partition complexes segregate within the volume of the nucleoid. *Nat. Commun.* 7:12107.

35. Schumacher, D., S. Bergeler, …, L. Søgaard-Andersen. 2017. The PomXYZ proteins self-organize on the bacterial nucleoid to stimulate cell division. *Dev. Cell.* 41:299–314.e13.

36. Uhía, I., M. Priestman, …, B. D. Robertson. 2018. Analysis of ParAB dynamics in mycobacteria shows active movement of ParB and differential inheritance of ParA. *PLoS One.* 13:e0199316.

37. Bouet, J.-Y., M. Bouvier, and D. Lane. 2006. Concerted action of plasmid maintenance functions: partition complexes create a requirement for dimer resolution. *Mol. Microbiol.* 62:1447–1459.

38. Guilhas, B., J.-C. Walter, …, M. Nollmann. 2020. ATP-driven separation of liquid phase condensates in bacteria. *Mol. Cell.* 79:293–303.e4.

39. Sanchez, A., D. I. Cattoni, …, J. Y. Bouet. 2015. Stochastic self-assembly of ParB proteins builds the bacterial DNA segregation apparatus. *Cell Syst.* 1:163–173.

40. Miller, J. H. 1972. Experiments in Molecular Genetics. Cold Spring Harbor Laboratory, Cold Spring Harbor, NY.

41. Lemonnier, M., J.-Y. Bouet, …, D. Lane. 2000. Disruption of the F plasmid partition complex in vivo by partition protein SopA. *Mol. Microbiol.* 38:493–505.

42. Diaz, R., J. Rech, and J.-Y. Bouet. 2015. Imaging centromere-based incompatibilities: insights into the mechanism of incompatibility mediated by low-copy number plasmids. *Plasmid.* 80:54–62.

43. Schindelin, J., I. Arganda-Carreras, …, A. Cardona. 2012. Fiji: an open-source platform for biological-image analysis. *Nat. Methods.* 9:676–682.

44. Ducret, A., E. M. Quardokus, and Y. V. Brun. 2016. MicrobeJ, a tool for high throughput bacterial cell detection and quantitative analysis. *Nat. Microbiol.* 1:16077.

45. Surovtsev, I. V., H. C. Lim, and C. Jacobs-Wagner. 2016. The slow mobility of the ParA partitioning protein underlies its steady-state patterning in Caulobacter. *Biophys. J.* 110:2790–2799.

46. Mori, H., Y. Mori, …, S. Hiraga. 1989. Purification and characterization of SopA and SopB proteins essential for F plasmid partitioning. *J. Biol. Chem.* 264:15535–15541.

47. Yates, P., D. Lane, and D. P. Biek. 1999. The F plasmid centromere, sopC, is required for full repression of the sopAB operon. *J. Mol. Biol.* 290:627–638.

48. Vecchiarelli, A. G., Y.-W. Han, …, K. Mizuuchi. 2010. ATP control of dynamic P1 ParA-DNA interactions: a key role for the nucleoid in plasmid partition. *Mol. Microbiol.* 78:78–91.

49. Morozov, A. Y., and A. B. Kolomeisky. 2007. Transport of molecular motor dimers in burnt-bridge models. *J. Stat. Mech*, arXiv, arXiv:0709.3529 https://arxiv.org/abs/0709.3529.

50. Saffarian, S., H. Qian, …, G. Goldberg. 2006. Powering a burnt bridges Brownian ratchet: a model for an extracellular motor driven by proteolysis of collagen. *Phys. Rev. E Stat. Nonlin. Soft Matter Phys.* 73:041909.

51. Adachi, S., K. Hori, and S. Hiraga. 2006. Subcellular positioning of F plasmid mediated by dynamic localization of SopA and SopB. *J. Mol. Biol.* 356:850–863.

52. Bouet, J.-Y., J. Rech, …, D. Lane. 2005. Probing plasmid partition with centromere-based incompatibility. *Mol. Microbiol.* 55:511–525.

53. Graham, T. G. W., X. Wang, …, J. J. Loparo. 2014. ParB spreading requires DNA bridging. *Genes Dev.* 28:1228–1238.

54. Rodionov, O., M. Łobocka, and M. Yarmolinsky. 1999. Silencing of genes flanking the P1 plasmid centromere. *Science.* 283:546–549.

55. Lynch, A. S., and J. C. Wang. 1995. SopB protein-mediated silencing of genes linked to the sopC locus of *Escherichia coli* F plasmid. *Proc. Natl. Acad. Sci. USA.* 92:1896–1900.

56. Goldenfeld, N. 1992. Lectures on Phase Transitions and the Renormalization Group. Addison-Wesley, Boca Raton, FL.

57. Frame, R., and J. O. Bishop. 1971. The number of sex-factors per chromosome in *Escherichia coli*. *Biochem. J.* 121:93–103.

58. Hopfield, J. J. 1994. Physics, computation, and why biology looks so different. *J. Theor. Biol.* 171:53–60.

59. Ietswaart, R., F. Szardenings, …, M. Howard. 2014. Competing ParA structures space bacterial plasmids equally over the nucleoid. *PLoS Comput. Biol.* 10:e1004009.

60. Bouet, J. Y., and B. E. Funnell. 1999. P1 ParA interacts with the P1 partition complex at parS and an ATP-ADP switch controls ParA activities. *EMBO J.* 18:1415–1424.

61. Figge, R. M., J. Easter, and J. W. Gober. 2003. Productive interaction between the chromosome partitioning proteins, ParA and ParB, is required for the progression of the cell cycle in *Caulobacter crescentus*. *Mol. Microbiol.* 47:1225–1237.

62. Osorio-Valeriano, M., F. Altegoer, …, M. Thanbichler. 2019. ParB-type DNA segregation proteins are CTP-dependent molecular switches. *Cell.* 179:1512–1524.e15.

63. Libante, V., L. Thion, and D. Lane. 2001. Role of the ATP-binding site of SopA protein in partition of the F plasmid. *J. Mol. Biol.* 314:387–399.

64. Hatano, T., Y. Yamaichi, and H. Niki. 2007. Oscillating focus of SopA associated with filamentous structure guides partitioning of F plasmid. *Mol. Microbiol.* 64:1198–1213.

65. Ah-Seng, Y., F. Lopez, …, J.-Y. Bouet. 2009. Dual role of DNA in regulating ATP hydrolysis by the SopA partition protein. *J. Biol. Chem.* 284:30067–30075.

66. Soh, Y.-M., I. F. Davidson, …, S. Gruber. 2019. Self-organization of *parS* centromeres by the ParB CTP hydrolase. *Science.* 366:1129–1133.

67. Jalal, A. S. B., N. T. Tran, and T. B. K. Le. 2020. ParB spreading on DNA requires cytidine triphosphate in vitro. *eLife.* 9:e53515.

68. Qian, H., P.-Z. Shi, and J. Xing. 2009. Stochastic bifurcation, slow fluctuations, and bistability as an origin of biochemical complexity. *Phys. Chem. Chem. Phys.* 11:4861–4870.

69. Ebersbach, G., S. Ringgaard, …, K. Gerdes. 2006. Regular cellular distribution of plasmids by oscillating and filament-forming ParA ATPase of plasmid pB171. *Mol. Microbiol.* 61:1428–1442.

70. Crowder, M. E., M. Strzelecka, …, R. Heald. 2015. A comparative analysis of spindle morphometrics across metazoans. *Curr. Biol.* 25:1542–1550.

71. West, G. B., and J. H. Brown. 2005. The origin of allometric scaling laws in biology from genomes to ecosystems: towards a quantitative unifying theory of biological structure and organization. *J. Exp. Biol.* 208:1575–1592.

72. Chan, Y.-H. M., and W. F. Marshall. 2012. How cells know the size of their organelles. *Science.* 337:1186–1189.

73. Willis, L., and K. C. Huang. 2017. Sizing up the bacterial cell cycle. *Nat. Rev. Microbiol.* 15:606–620.

74. Si, F., G. Le Treut, …, S. Jun. 2019. Mechanistic origin of cell-size control and homeostasis in bacteria. *Curr. Biol.* 29:1760–1770.e7.

75. Chen, J., and J. Liu. 2016. Spindle size scaling contributes to robust silencing of mitotic spindle assembly checkpoint. *Biophys. J.* 111:1064–1077.

76. MacCready, J. S., P. Hakim, …, D. C. Ducat. 2018. Protein gradients on the nucleoid position the carbon-fixing organelles of cyanobacteria. *eLife.* 7:e39723.

77. Vecchiarelli, A. G., K. Mizuuchi, and B. E. Funnell. 2012. Surfing biological surfaces: exploiting the nucleoid for partition and transport in bacteria. *Mol. Microbiol.* 86:513–523.

78. Fogel, M. A., and M. K. Waldor. 2006. A dynamic, mitotic-like mechanism for bacterial chromosome segregation. *Genes Dev.* 20:3269–3282.

79. Marston, A. L., and J. Errington. 1999. Dynamic movement of the ParA-like Soj protein of B. subtilis and its dual role in nucleoid organization and developmental regulation. *Mol. Cell.* 4:673–682.

80. Schofield, W. B., H. C. Lim, and C. Jacobs-Wagner. 2010. Cell cycle coordination and regulation of bacterial chromosome segregation dynamics by polarly localized proteins. *EMBO J.* 29:3068–3081.

81. Feddersen, H., L. Würthner, …, M. Bramkamp. 2021. Dynamics of the Bacillus subtilis Min system. *MBio.* 12:e00296-21.

82. de Boer, P. A., R. E. Crossley, and L. I. Rothfield. 1989. A division inhibitor and a topological specificity factor coded for by the minicell locus determine proper placement of the division septum in *E. coli*. *Cell.* 56:641–649.

83. Marston, A. L., H. B. Thomaides, …, J. Errington. 1998. Polar localization of the MinD protein of Bacillus subtilis and its role in selection of the mid-cell division site. *Genes Dev.* 12:3419–3430.

84. Hughes, K. T. 2017. Flagellum length control: how long is long enough? *Curr. Biol.* 27:R413–R415.

85. Keener, J. P. 2006. How Salmonella Typhimurium measures the length of flagellar filaments. *Bull. Math. Biol.* 68:1761–1778.

Biophysical Journal, Volume *120*

Supplemental information

Spatial control over near-critical-point operation ensures fidelity of Par-ABS-mediated DNA partition

Longhua Hu, Jérôme Rech, Jean-Yves Bouet, and Jian Liu

SUPPLEMENTAL INFORMATION

LH Hu, J Rech, JY Bouet, J Liu

SECTION I. MODEL PARAMETER TABLE

Table S1

Parameter	Physical meaning	Value range	Nominal chosen value	Reference
k_{nl}	Nucleoid elongation rate	6 – 18 nm/min	12 nm/min	Our exp
k_{syn}	ParA synthesis rate	0 – 100 /min	30 /min	Estimated from (1, 2) & our exp
k_{on}	Rate of ParA-ParB bond formation	10^3 – 10^4/sec	3300/sec	Estimated from (3)
k_{off}	Rate of ParA-ParB bond dissociation	~ 1.0/sec	1.0/sec	(4, 5)
k_a	Rate of cytosolic ParA·ATP binding to nucleoid	0.01–5.0/sec	3.0/sec	(3-7)
k_n	Rate of $ParA^D$ conversion to ParA·ATP	~ 0.1/sec	0.1/sec	(3)
$k_{d,T}$	Rate of ParA·ATP-nucleoid dissociation	~ 0.01/sec	0.01/sec	(4, 5)
$k_{d,D}$	Rate of $ParA^D$-nucleoid dissociation	~ 5.0/sec	5.0/sec	(4, 5)
D_p	Diffusion constant of PC	~ 10^3 -10^4 nm^2/sec	10^4 nm^2/sec	(8)
$D_{T,N}$	Diffusion constant of ParA·ATP along nucleoid	(1-5)×10^3 nm^2/sec	1250 nm^2/sec	(5, 9)
$D_{D,N}$	Diffusion constant of $ParA^D$ along nucleoid	(1-5)×10^3 nm^2/sec	1250 nm^2/sec	(5, 9)
$D_{T,C}$	Diffusion constant of cytosolic ParA·ATP	~ 10^5 nm^2/sec	10^5 nm^2/sec	(5, 9)
$D_{D,C}$	Diffusion constant of cytosolic $ParA^D$	10^3 nm^2/sec	10^3 nm^2/sec	(5, 9)
K_S	Spring constant of ParA-ParB bond	0.2 pN/nm	0.2 pN/nm	Estimated in (10, 11)
R	Radius of PC	100 nm	100 nm	(1, 12)
ρ_B	ParB density on PC	~0.013/nm^2	0.013/nm^2	(1)
L_e	Equilibrium ParA-ParB bond length	50 nm	50 nm	Estimated in (11, 13)
L_a	Maximal length for a newly formed bond	53 nm	53 nm	Estimated in (11, 13)
L_m	Maximal bond length extension	10 nm	10 nm	Estimated in (11, 13)
$k_{d,\ plasmid}$	Rate of PC-bound ParA·ATP dissociation	~ 5.0/sec	5.0/sec	

$k_{\text{a, plasmid}}$	Rate of cytosolic ParA·ATP-PC association	10 - 1000/sec	100.0/sec	
N_C^{PC}	Upper limit of PC-localized ParA number	100-1500	500	(4, 5)
k_a'	Rate of PC-bound ParA re-binding to nucleoid	$< k_a$	0.3/sec	(4, 5)

Note: The current model is built upon our established models (11, 13), in which we have done extensive parameter sensitivity test for most of the model parameters (*i.e.*, those in the Table S1 that are not in shaded box). These parameter sensitivity tests suggest that the essential features of the model – including those presented in Figs. 2 and 4 this paper – can be preserved in a broad range of model parameter space. The new ingredients in our current model pertain to the PC-localization of ParA, whose effects are characterized by the model parameters in shaded box in the Table S1. We have extended our parameter sensitivity tests to these parameters, the results of which are formulated as the model phase diagrams in Fig. 5C in the main text and Fig. S4 in the Section II (see below).

SECTION II. SUPPLEMENTAL FIGURES

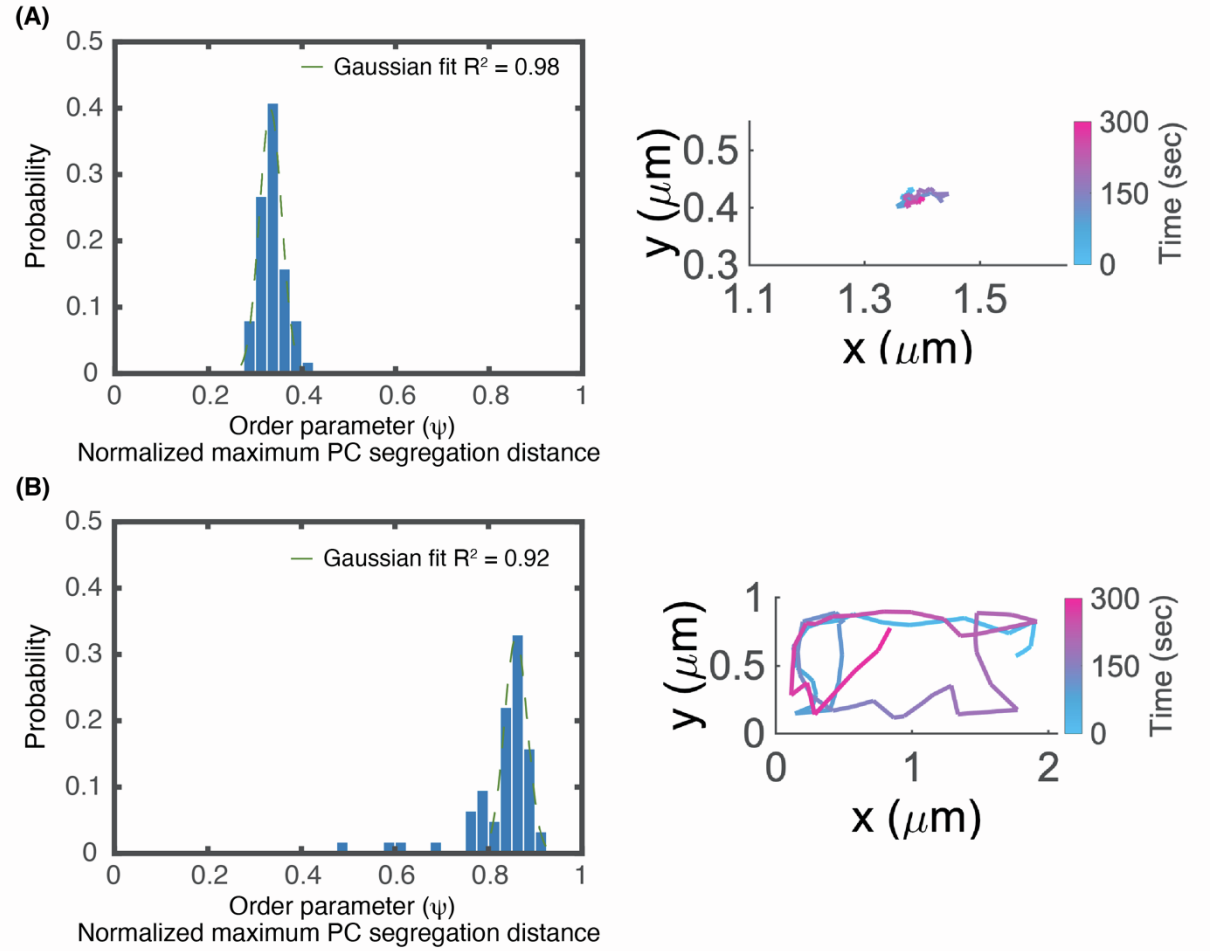

Fig. S1. Statistical distributions of order parameter, ψ (left) and representative simulation trajectories of PC movement (right) in the parameter regimes away from the critical point. (A) Near-static case (deep in the directed segregation regime). (B) Pole-to-pole oscillation. Note that, we calculated 1) the χ^2-value between the cumulative distribution function (CDF) of our data and Gaussian distribution and 2) the excess kurtosis values for (A) and (B). For the near-static case in (A), the χ^2-value and excess kurtosis value are 3.0 and -0.4, respectively. This suggests that the near-static case is closer to a Gaussian distribution than the case at the critical point in Figs. 2C and 2D, whose corresponding statistical measures are 6.6 and -1.0, respectively. In comparison, for the pole-to-pole oscillation in (B) the χ^2-value and excess kurtosis value are 21.0 and 8.0, respectively. This analysis result indicates that the excursion distribution in pole-to-pole oscillation is even more non-Gaussian than the case at the critical point. This is because, the excursion distribution of pole-to-pole oscillation has a long tail, which stems from the cases that the two PCs either have head-on collision and/or travel together, as shown in our previous work (13). Although the PCs move back and forth between the two poles for most of the time, these entanglements hinder the PC excursion and thus skew the distribution. As we previously suggested (13), because the two PCs are susceptible to traveling together if the partition machinery operates in the pole-to-pole oscillation regime, the partition fidelity (*i.e.*, the probability of having the two PCs in the two different cell halves) is predicted to be highly variable. This could explain the observation that only ~ 1% of *E. coli* displays pole-to-pole oscillation in low-copy plasmid partition, further

suggesting that the operating point of ParAB*S* system could be shaped by evolution to maximize the partition fidelity.

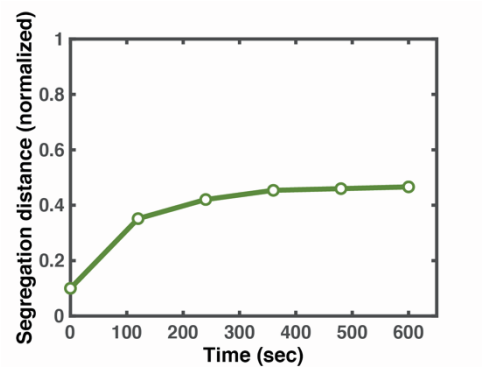

Fig. S2. PC segregation distance over time. Here, an example is provided to show that PC segregation distance (operating at the critical point in Fig. 2C) has already reached the steady state at t =10 minutes. As such, our analysis is not expected to change much for a longer simulation. Additionally, we used 10-min of simulation run to faithfully compare with our experimental data, which is also 10-min in duration.

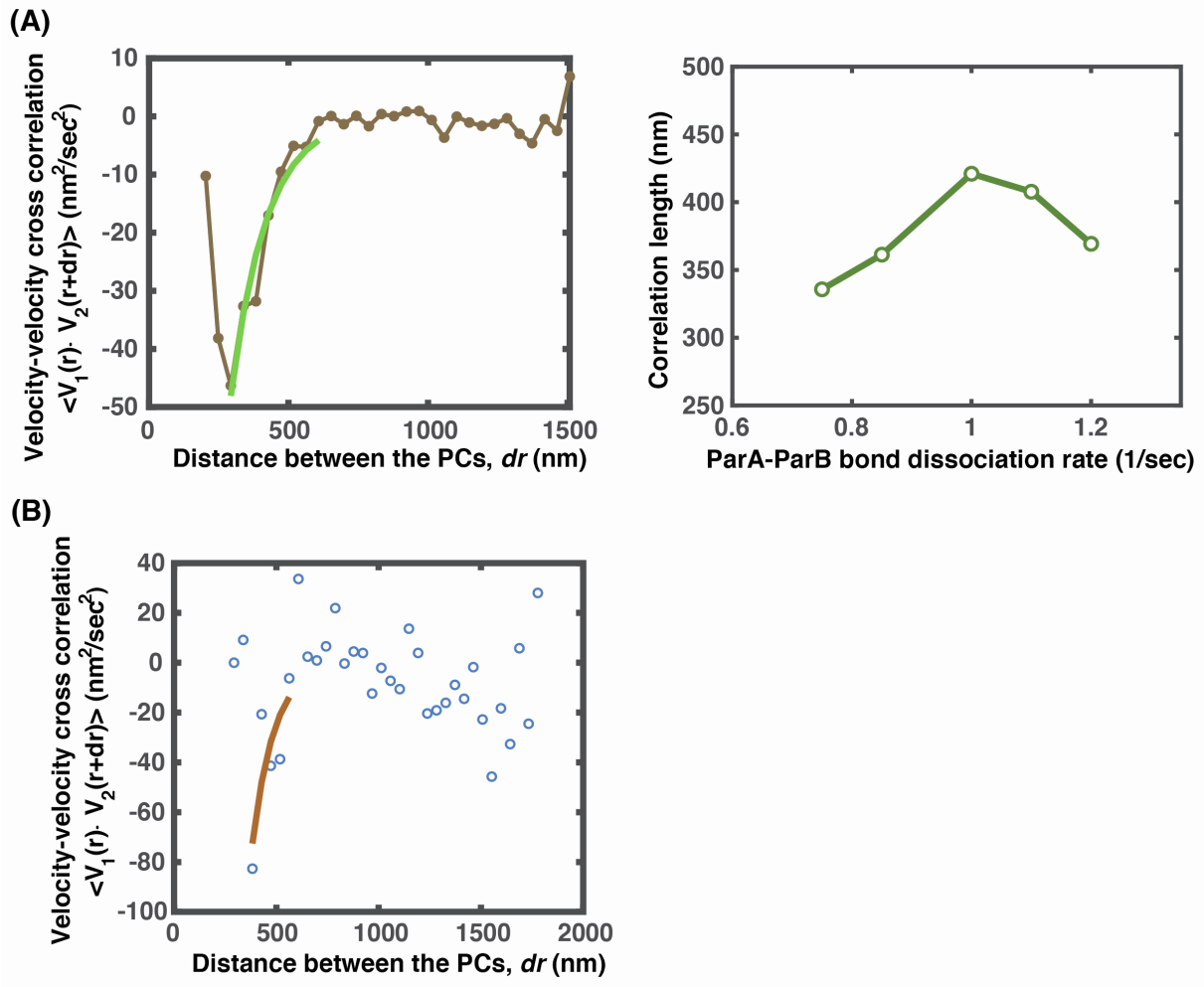

Fig. S3. Correlation function of PC movements. (A) Model result. Left: Cross-correlation function of PC movements vs. distance between the PCs for the case at the critical point. Right: Plot of correlation length vs. k_{off}. It shows that the correlation length peaks (~ 400 nm) at the critical point. (B) Experimental data of cross-correlation function of PC movement vs. distance. The correlation length of PC movement is determined to be ~ 500 nm. For (A) and (B), the velocity cross correlation function is calculated from $\langle \vec{V}_1(r) \cdot \vec{V}_2(r+dr) \rangle$, where the subscripts 1 and 2 denotes the pair of PCs in a cell, separated by the distance between the PCs, *dr*, and the <...> denotes the ensemble average. Additionally, the ensemble average is over 64 and 60 pairs of PCs for the model result (A) and for the experiment (B), respectively. The correlation function displays a peak of negative value at some distances, indicating that the movements of PCs are correlated when they undergo directed segregation. To compute the correlation length, the decreasing part of the peak is fit with the exponential function a·exp(-dr/L_C) (*i.e.*, the green curve in (A) and the brown curve in (B)), which yields the characteristic length L_C. The peak occurs at the distance L_P due to the excluded volume effect between the PCs. The correlation length is $L_C + L_P$, the sum of the characteristic length, L_C and the peak position, L_P.

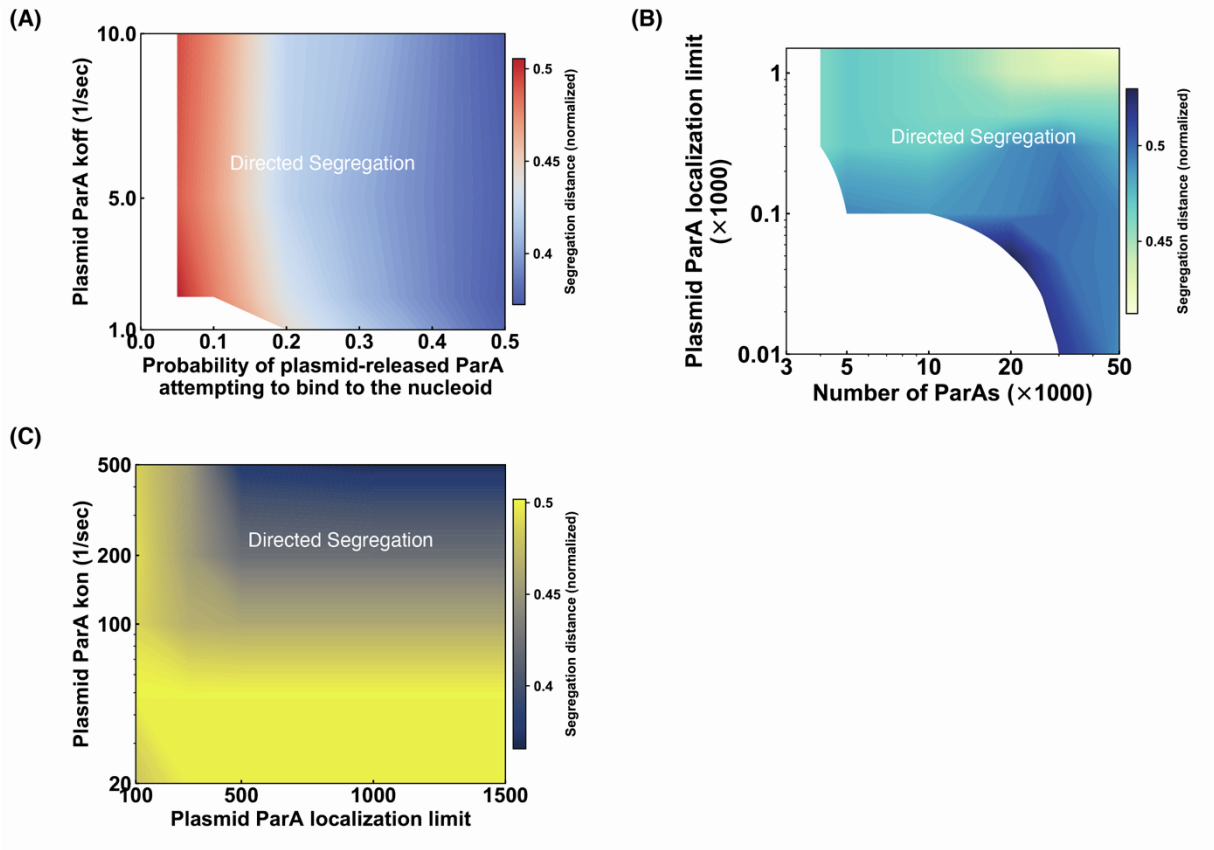

Fig. S4. Model phase diagram studies of PC-ParA localization effects on PC partitioning. (A) ParA turnover rate from PC vs. percentage of PC-released ParA that binds to nucleoid. (B) Saturation level of PC-localized ParA vs. total ParA number. (C) ParA binding rate onto PC vs. Saturation level of PC-localized ParA. For (A-C): We varied the two parameters in the respective phase diagrams, while keeping the rest of the model parameters fixed in accordance with the nominal chosen values in the Table S1. For each point in the phase diagram, we ran stochastic simulations for ≥ 36 trajectories of 10 min-dynamical evolution of the system, starting from the same initial condition and parameter set. The segregation distance reports the average value of ≥ 36 trajectories at the end of the simulation.

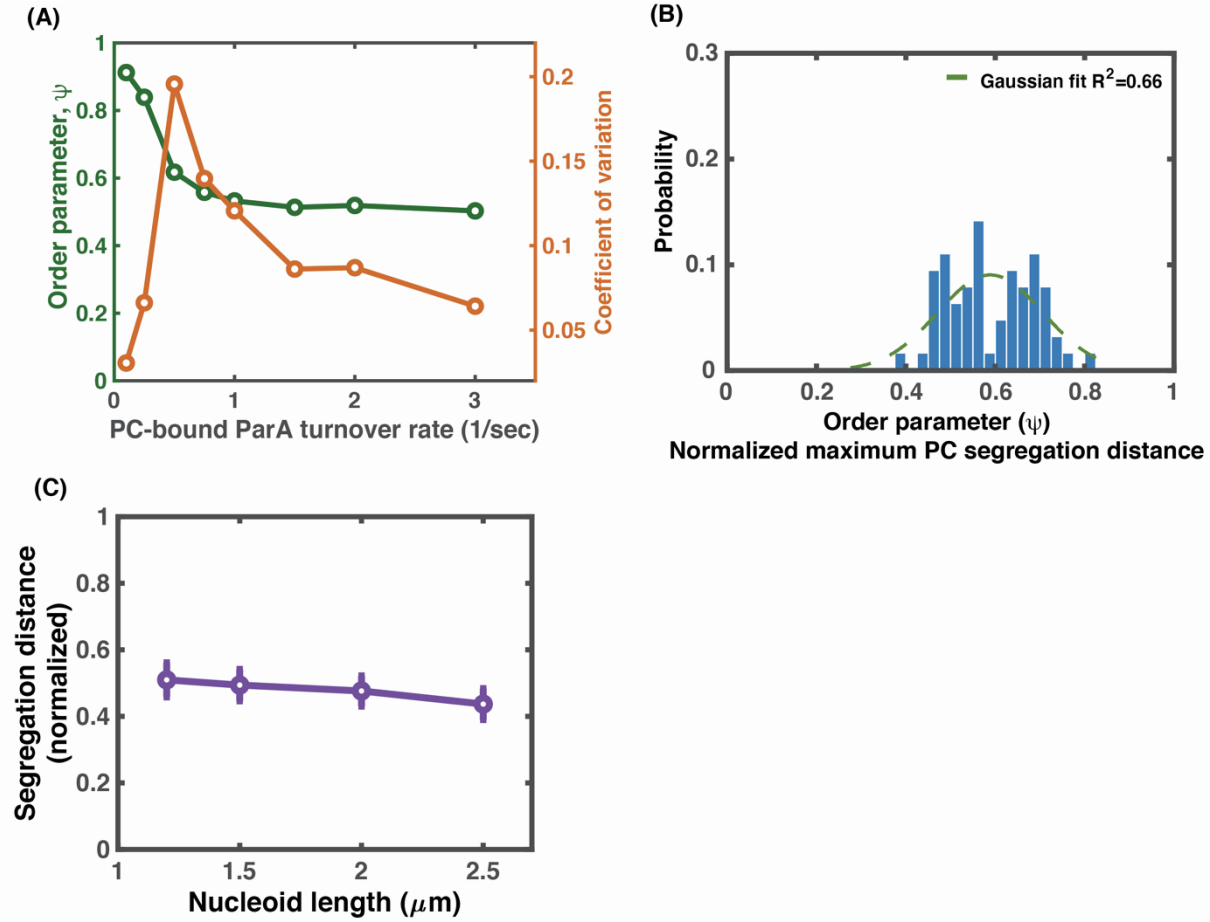

Fig. S5. Full model with PC-localization of ParA preserves all the essence of near-tipping-point partition as that in Fig. 2. (A) Order parameter and its variation as functions of PC-bound ParA turnover rate. (B) Statistical distribution of the order parameter, ψ, near the critical point. (C) Segregation distance adapts to half of the nucleoid lengths near the tipping point in the parameter space. The parameter set ($k_{a,\,plasmid}$, $k_{off,\,plasmid}$) used here is the same as that in Fig. 5B.

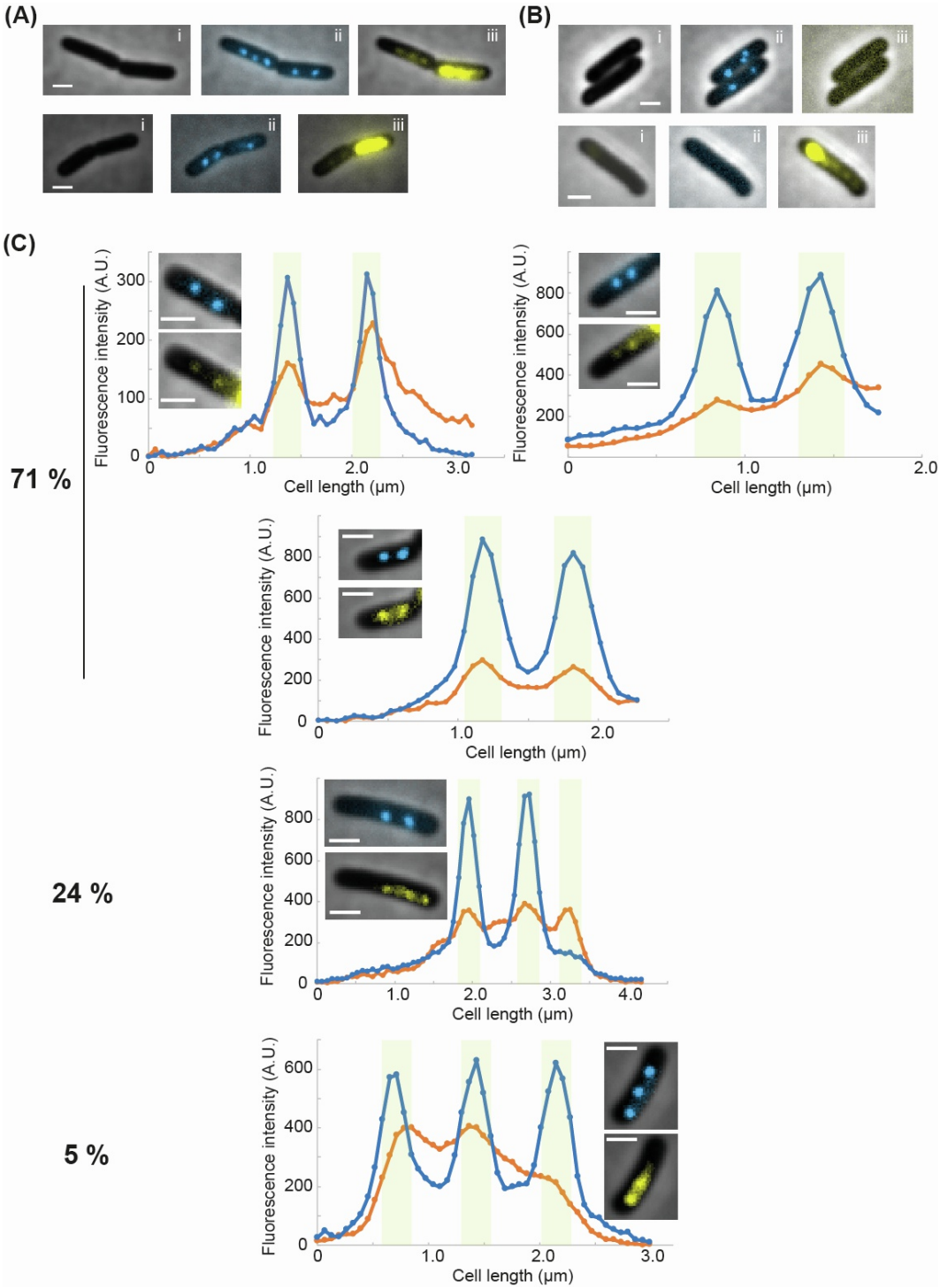

Fig. S6. Co-localization of $ParA_F$ foci and partition complexes. (A) Two typical examples of asymmetric inheritance of $ParA_F$ upon cell division. Due to the oscillatory behavior of $ParA_F$, most often one cell inherits most of $ParA_F$ while the other a much smaller amount. Dividing cells are observed in phase contrast (i) and in fluorescence microcopy to observe $ParB_F$-mTq2 (ii, blue channel) or $ParA_F$-mVenus (iii, yellow channel) in overlay with phase contrast. Cells were grown at 30°C in MGlyC. (B) Fluorescence signals are specifically detected without spreading in other channels. Strains carrying mini-F plasmids expressing either only $ParB_F$-mTurquoise (pJYB240; top) or only $ParA_F$-mVenus (pJYB243, bottom) are grown and imaged as in (A). No leaky signal from mTurquoise2 or mVenus is observed in the yellow (iii) or blue (ii) channels, respectively. (C) Line scan analyses of fluorescence intensity

along cell length. Blue and orange lines correspond to the blue ($ParB_F$-mTq2) and yellow ($ParA_F$-mVenus) channels, respectively. The corresponding cell images is displayed in the graph as in (A). Over 58 cells, 41 (71%) displayed the same number of ParA and ParB foci, 14 (24%) displayed more ParA than ParB foci, and 3 (5%) displayed more ParB than ParA foci. The light green area corresponds to the limit of resolution of the microscope (i.e. 4 pixels (262 nm) around the PC peaks). Scale bar: 1 μm in all images.

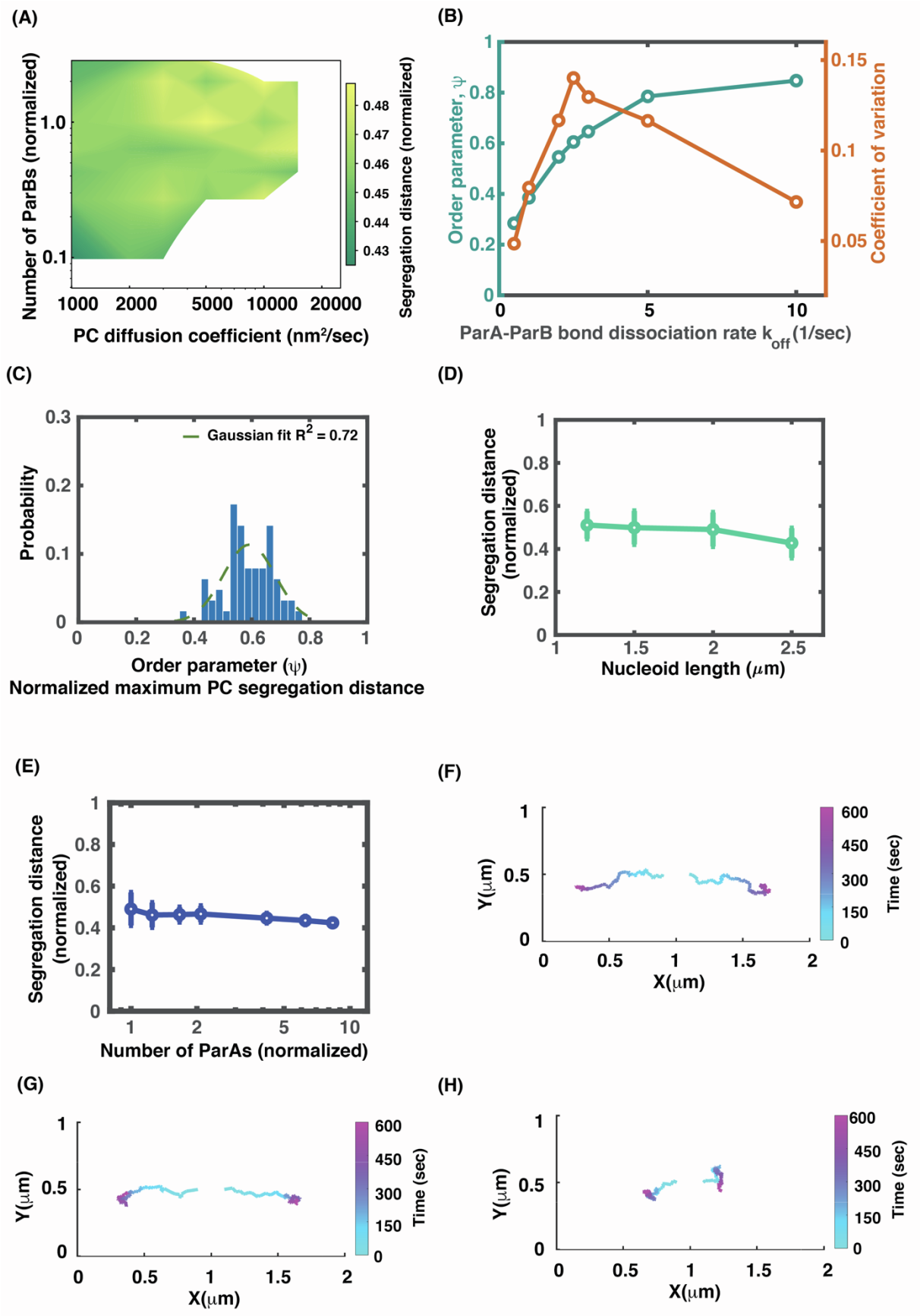

Fig. S7. Model exploration of potential impacts of PC moving inside nucleoid on PC partition. The explored effects include the combination of a slower PC diffusion and variation

in the number of PC-bound ParB available for ParA binding (A-E), and non-uniform nucleoid DNA distribution (F-H). Here, all the model calculations are performed with the full model that depicts the PC-localization of ParA. (A) Computed phase diagram of the dependence of PC segregation on PC diffusion coefficients and the number of PC-bound ParBs that is available for ParA binding. (B) Characteristics of the near-tipping-point operation. (C) Statistical distribution of order parameter, ψ, near the critical point. (D) The segregation distance adapts to half-lengths of the nucleoid near the tipping point. The parameter set of ($k_{a,\ plasmid}$, $k_{off,\ plasmid}$) used here is the same as that in Fig. 5B. (E) Segregation distance adaptation buffers against the variations in the ParA level. For (B-E), the PC diffusion coefficient is chosen to be 2000 nm^2/sec, 5 times slower than that in Fig. 5. (F-H) Non-uniform nucleoid DNA density directs PC movement. PCs move on the nucleoid substrate surface with non-uniform DNA density along the x-direction. Three cases were simulated: (F) the density of nucleoid DNA increases from the center to the poles; (G) the density of nucleoid DNA increases from the center to the quarter positions; and (H) the density of nucleoid DNA decreases from the center to the poles. A typical simulated trajectory is shown for each case, and normalized segregation distance averaged over 36 independent trajectories are (F) 0.69, (G) 0.63 and (H) 0.27, respectively.

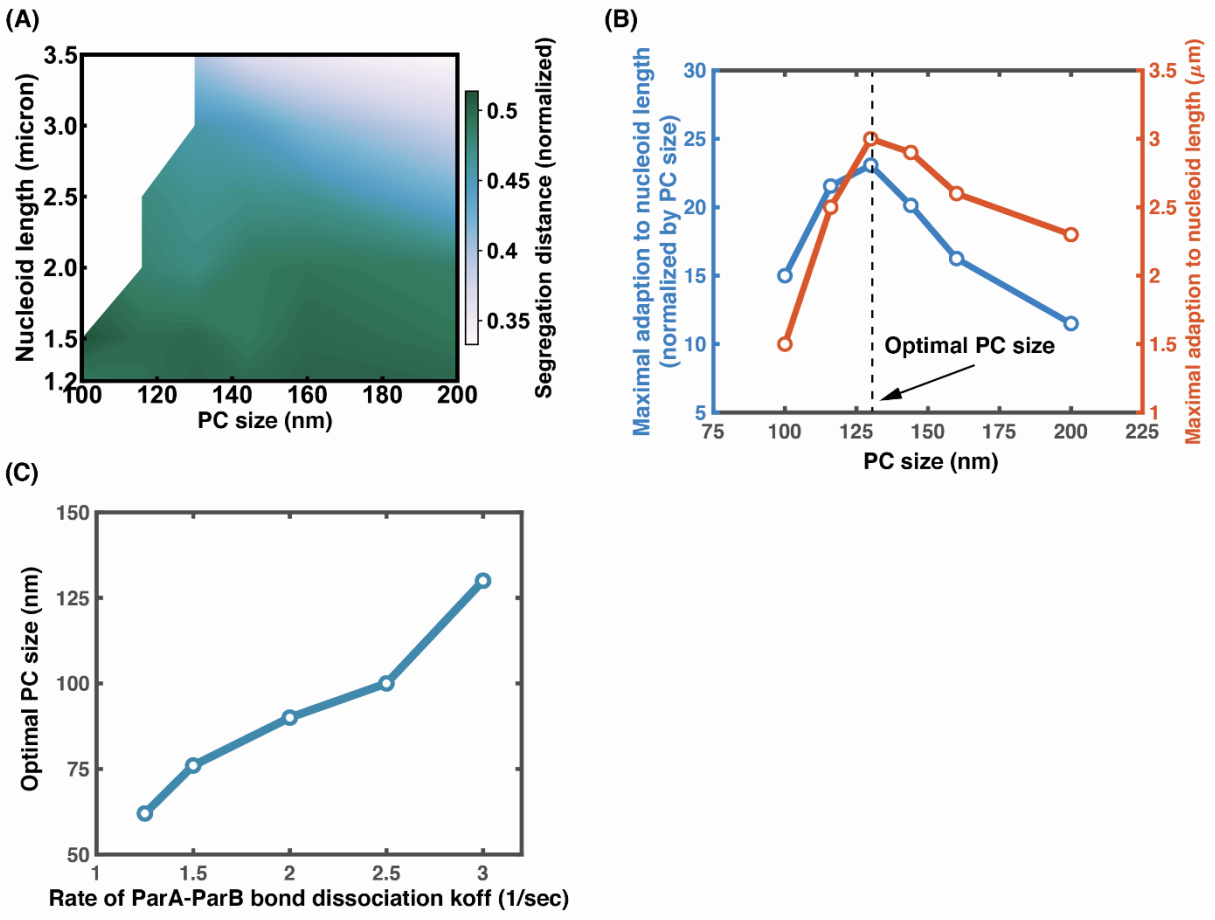

Fig. S8. Spatial control over near tipping-point operation defines an optimal PC size for maximal partition adaptation of nucleoid length. (A) Nucleoid length vs. PC size. The color bar represents the relative PC segregation distance, i.e., the PC segregation distance divided by the nucleoid length at 10-min time mark. (B) Maximal nucleoid length of partition adaptation vs. PC size. We used the relative PC segregation distance of 0.45 as the threshold, above which we termed the PC partition as being faithful. As such, the maximal nucleoid length at a given PC size is defined as the longest nucleoid length for faithful partition of the corresponding PC. While keeping all other model parameters fixed, we varied the PC size along with 1) the corresponding maximum number of PC-localized ParA (i.e., proportional to the PC surface area) and 2) diffusion coefficient of PC (*i.e.*, proportional to the inverse of PC diameter). (C) ParA-ParB bond dissociation rate vs. optimal PC size. To obtain this curve, we varied k_{off} near the transition line between "pole-to-pole oscillation" and "directed segregation" in the phase diagram of Fig. 2A, and then repeated the calculation in (B) to determine the corresponding optimal PC size.

SECTION III. SUPPLEMENTAL REFERENCE

1. Sanchez, A., Diego I. Cattoni, J.-C. Walter, J. Rech, A. Parmeggiani, M. Nollmann, and J.-Y. Bouet. 2015. Stochastic Self-Assembly of ParB Proteins Builds the Bacterial DNA Segregation Apparatus. Cell Systems 1(2):163-173.
2. Yates, P., D. Lane, and D. P. Biek. 1999. The F plasmid centromere, sopC, is required for full repression of the sopAB operon. Journal of Molecular Biology 290(3):627-638.
3. Vecchiarelli, A. G., Y.-W. Han, X. Tan, M. Mizuuchi, R. Ghirlando, C. Biertümpfel, B. E. Funnell, and K. Mizuuchi. 2010. ATP control of dynamic P1 ParA–DNA interactions: a key role for the nucleoid in plasmid partition. Molecular Microbiology 78(1):78-91.
4. Hwang, L. C., A. G. Vecchiarelli, Y. W. Han, M. Mizuuchi, Y. Harada, B. E. Funnell, and K. Mizuuchi. 2013. ParA‐mediated plasmid partition driven by protein pattern self‐organization. The EMBO Journal 32(9):1238-1249.
5. Vecchiarelli, A. G., L. C. Hwang, and K. Mizuuchi. 2013. Cell-free study of F plasmid partition provides evidence for cargo transport by a diffusion-ratchet mechanism. Proceedings of the National Academy of Sciences 110(15):E1390-E1397.
6. Castaing, J.-P., J.-Y. Bouet, and D. Lane. 2008. F plasmid partition depends on interaction of SopA with non-specific DNA. Molecular Microbiology 70(4):1000-1011.
7. Hatano, T., and H. Niki. 2010. Partitioning of P1 plasmids by gradual distribution of the ATPase ParA. Molecular Microbiology 78(5):1182-1198.
8. Vecchiarelli, A. G., K. C. Neuman, and K. Mizuuchi. 2014. A propagating ATPase gradient drives transport of surface-confined cellular cargo. Proceedings of the National Academy of Sciences 111(13):4880-4885.
9. Surovtsev, Ivan V., Hoong C. Lim, and C. Jacobs-Wagner. 2016. The Slow Mobility of the ParA Partitioning Protein Underlies Its Steady-State Patterning in Caulobacter. Biophysical Journal 110(12):2790-2799.
10. Bustamante, C., S. B. Smith, J. Liphardt, and D. Smith. 2000. Single-molecule studies of DNA mechanics. Current Opinion in Structural Biology 10(3):279-285.
11. Hu, L., A. G. Vecchiarelli, K. Mizuuchi, K. C. Neuman, and J. Liu. 2015. Directed and persistent movement arises from mechanochemistry of the ParA/ParB system. Proceedings of the National Academy of Sciences 112(51):E7055-E7064.
12. Lim, H. C., I. V. Surovtsev, B. G. Beltran, F. Huang, J. Bewersdorf, and C. Jacobs-Wagner. 2014. Evidence for a DNA-relay mechanism in ParABS-mediated chromosome segregation. eLife 3:e02758.
13. Hu, L., A. G. Vecchiarelli, K. Mizuuchi, K. C. Neuman, and J. Liu. 2017. Brownian Ratchet Mechanism for Faithful Segregation of Low-Copy-Number Plasmids. Biophysical Journal 112(7):1489-1502.